

University of Nebraska - Lincoln

DigitalCommons@University of Nebraska - Lincoln

Mechanical (and Materials) Engineering --
Dissertations, Theses, and Student Research

Mechanical & Materials Engineering,
Department of

11-2019

Double-sided corrugated composite tube and axle protective mechanism for railway vehicles

Hozhabr Mozafari

Follow this and additional works at: <https://digitalcommons.unl.edu/mechengdiss>



Part of the [Materials Science and Engineering Commons](#), and the [Mechanical Engineering Commons](#)

This Article is brought to you for free and open access by the Mechanical & Materials Engineering, Department of at DigitalCommons@University of Nebraska - Lincoln. It has been accepted for inclusion in Mechanical (and Materials) Engineering -- Dissertations, Theses, and Student Research by an authorized administrator of DigitalCommons@University of Nebraska - Lincoln.

**Double-sided corrugated composite tube and axle protective mechanism for railway
vehicles**

By

Hozhabr Mozafari

A THESIS

Presented to the Faculty of

The Graduate College at the University of Nebraska

In Partial Fulfillment of Requirements

For the Degree of Master of Science

Major: Mechanical Engineering and Applied Mechanics

Under the Supervision of Professor Linxia Gu

Lincoln, Nebraska

December 2019

Double-sided corrugated composite tube and axle protective mechanism for railway vehicles

Hozhabr Mozafari, M.S.

University of Nebraska, 2019

Advisor: Linxia Gu

Structural elements in transportation vehicles are exposed to different types of dynamic loadings and impact scenarios. Protecting passengers against injury and providing mechanisms to avoid impact induced damages to the critical components are the two hot topics in crashworthiness engineering. The presented research work includes two parts. The first part is about designing a novel double-sided composite corrugated tube that can be implemented in front chassis rail of ground vehicles to improve their crashworthiness against collision and car accidents. To maximize the controllable energy absorption of corrugation troughs as observed in the single sided corrugated (SSC) tube, we proposed and tested a new structure design, i.e., double-sided corrugated (DSC) tube made of Al 6060-T6 aluminum alloy or CF1263 carbon/epoxy composite. Finite element models were developed to test the DSC tube in comparison with both SSC and classical straight (S) tubes under axial crushing. Results have shown that the total absorbed energy of the DSC aluminum tube with 14 corrugations was 330% and 32% higher than that of the SSC tube with 14 corrugations and the S-tube, respectively. The second part of this research work is about designing a novel protective mechanism for railway car axle against ballast impact. The ice detached from the train body can fall on the track and form projectiles of ice and gravel (ballast); sharp, heavy, and at high impact energy. The main preventive mechanism

in many countries such as Norway is to use protective coating on the axle. But when the coating is damaged by impact, bare steel of the axle can be exposed. The corrosion of these exposed impact zones can cause pits and cavities that become points of stress concentration where fatigue cracks can develop. Due to the current problems with coating technique we suggested a novel protective mechanism and used sandwich panel to protect railway axle against impact. Our results showed that the device can dissipate more than 70 % of impact energy without introducing any damage to the axle surface. Moreover, the rebounding velocity of projectile reduced by 97 % which eliminates the risk of second impact to the other vehicle components. The suggested device can be mounted by using a simple clamping system and unmount easily for potential inspections.

DEDICATION

To my Beloved Parents,

To my dear Brother and Sister

Acknowledgements

Foremost, I would like to express my sincere gratitude and appreciation to professor Linxia Gu for the kind and enduring assistance and guidance through the course of this research. I would like to express my appreciation to Dr. Gabriella Epasto from Department of Engineering - University of Messina and Professor Emanoil Linul from Department of Mechanics and Strength of Materials, Politehnica University of Timisoara for their collaboration. I would like to thank Dr. Carl Nelson and Dr. Lucia Fernandez-Ballester for serving as graduate committee members. I would like to thank my colleagues that guided me with their constructive comments.

Table of contents

| | |
|---|----|
| Chapter 1: Literature review | 1 |
| 1.1 Introduction | 2 |
| 1.2 Crashworthiness and Impact integrity | 2 |
| 1.2.1 Crashworthiness and structures..... | 3 |
| 1.3 Energy absorption by irreversible deformation..... | 4 |
| 1.3.1 Properties of energy absorber device | 5 |
| 1.4 Types of crushing energy absorbers..... | 8 |
| 1.4.1 Metallic thin-walled structures | 8 |
| 1.4.2 Polymeric and Metallic Foams | 14 |
| 1.5 The target structural components | 15 |
| 1.5.1 Longitudinal crash rails (front chassis rails)..... | 15 |
| 1.5.2 Railway Axle | 16 |
| Chapter 2: Double sided composite corrugated tube | 20 |
| 2.1 Introduction | 21 |
| 2.2 Development of the FE model for thin-walled tubes | 21 |
| 2.4 Verification of FE model..... | 23 |

| | | |
|--|--|----|
| 2.5 | Mechanical advantage of double-sided corrugated tube | 24 |
| 2.6 | Composite DSC-14 tube..... | 31 |
| 2.7 | Effect of corrugation spacing on the performance of the DSC tube | 32 |
| Chapter 3: Ballast impact protection mechanism | | 35 |
| 3.1 | Introduction | 36 |
| 3.2 | Sandwich panel | 36 |
| 3.2.1 | Core material..... | 37 |
| 3.2.2 | Skin material | 39 |
| 3.3 | Finite Element Simulation..... | 40 |
| 3.3.1 | Modeling..... | 40 |
| 3.3.2 | Results..... | 42 |
| 3.4 | Experimental tests | 49 |
| Chapter 4: Conclusion..... | | 54 |

List of Figures

| | |
|--|----|
| Figure 1-1 Comparison of vehicle deformations from the NCAP frontal crash tests of; (a) Yaris and (c) Silverado, with the numerical models (b, d) [2] | 3 |
| Figure 1-2 Front chassis rails as an energy absorbing device [4] | 4 |
| Figure 1-3 An ideal energy absorber and its response under crushing load [5] | 6 |
| Figure 1-4 Typical load-displacement diagram for a thin-walled tubular energy absorber under axial crushing load [7] | 7 |
| Figure 1-5 Models of axisymmetric deformation in concertina mode | 9 |
| Figure 1-6 (a) axisymmetric mode; (b) non-symmetric mode; (c) mixed mode of axial crushing [14] | 10 |
| Figure 1-7 (a) Deformation mode and (b) force–deformation curve of a rectangular tube under axial crushing load [19] | 11 |
| Figure 1-8 conical crush energy absorbers with different cone angles [28] | 13 |
| Figure 1-9 Crushing response of the conical tube [29] | 13 |
| Figure 1-10 A typical nominal stress-strain curve for foam materials [5] | 14 |
| Figure 1-11 A brief overview of some key body structure elements [31] | 16 |
| Figure 2-1 Three-dimensional tube configurations. Left, Straight tube with constrains; Middle, single-sided corrugated tube with corrugation parameters; Right, double-sided corrugated tube | 21 |
| Figure 2-2 Load-displacement response of S tube for different element sizes | 23 |
| Figure 2-3 Load-displacement diagrams of the tubes under axial compressive loading .. | 24 |
| Figure 2-4 Equivalent Plastic Strain (PEEQ) contours. (a) S tube: Left, first fold initiation at crushing displacement of 0.37 mm; Middle, second fold development at displacement of | |

| | |
|---|----|
| 31.75 mm; Right, final compressed state with crushing displacement of 97.83; (b) SSC-14 tube: Left, first fold initiation at crushing displacement of 17 mm; Middle, second fold development at displacement of 27.7 mm; Right, final compressed state with crushing displacement of 89 mm; (c) DSC-14 tube: Left, first fold initiation at crushing displacement of 11 mm; Middle, second fold development at displacement of 23.5 mm; Right, final compressed state at crushing displacement of 79.8 mm. | 26 |
| Figure 2-5 Folding schematics of DSC-14 (top) and SSC-14 (bottom). | 27 |
| Figure 2-6 The (PEEQ) history at one specific region (first formed wrinkle) for S, SSC-14 and DSC-14 tubes. | 28 |
| Figure 2-7 Crushing progression of DSC-14 (Top) and SSC-14 tube (Bottom). | 28 |
| Figure 2-8 Crashworthiness properties of tube structures. | 31 |
| Figure 2-9 Corrugation spacing affect the crushing responses of DSC tubes. | 33 |
| Figure 2-10 Crushing progression of DSC-6 tube. | 34 |
| Figure 3-1 The prepared aluminum samples for quasi-static compression tests | 37 |
| Figure 3-2 The stress-strain diagram of aluminum foam cores | 38 |
| Figure 3-3 The aluminum sheets for preparing the sandwich panel skin | 39 |
| Figure 3-4 Finite element model of the impact analysis; (a) Railway axle model and the cutting planes; (b) the selected section of the axle covered with absorber; (c) The dimension of striker (mm). | 41 |
| Figure 3-5 The meshed model of axle and absorber..... | 42 |
| Figure 3-6 Equivalent plastic strain (PEEQ) for each case after the impact | 44 |
| Figure 3-7 Kinetic energy of the projectile during the impact simulation..... | 45 |
| Figure 3-8 Plastic dissipated energy during impact..... | 46 |

| | |
|---|----|
| Figure 3-9 Variation of projectile velocity during impact simulation | 46 |
| Figure 3-10 PEEQ variation through the thickness of absorber | 47 |
| Figure 3-11 The induced stress (top) and PEEQ (bottom) on the axle without absorber . | 49 |
| Figure 3-12 The Impact test setup | 50 |
| Figure 3-13 The cross section of samples with core thickness of 35 mm (top); the samples after impact tests (bottom) | 51 |
| Figure 3-14 Load-displacement curves of the tested sandwich panels..... | 52 |
| Figure 3-15 The velocity of impactor versus impact duration..... | 53 |
| Figure 4-1 Application of Double-sided composite corrugated tube in railway application [54]..... | 56 |
| Figure 4-6 The assembly of ballast impact absorber and clamping system | 57 |

List of Tables

| | |
|--|----|
| Table 2-1 Mechanical properties of laminate composite material CF1263..... | 22 |
| Table 3-1 The mechanical properties of tested foams in preliminary stage | 38 |
| Table 3-2 Mechanical properties of Aluminum alloy 6082 [52] | 39 |
| Table 3-3 The sample specifications for experimental tests..... | 49 |
| Table 3-4 The results of impact tests | 52 |

Chapter 1: Literature review

1.1 Introduction

This chapter covers the background literature and explains the important concepts which are related to this research. All reviewed materials are mentioned here to build a basis for understanding of the current research. This section will be presented in the following sub-sections:

- Crashworthiness and impact integrity
- Energy absorption by irreversible deformation
- Types of crushing energy absorbers

1.2 Crashworthiness and Impact integrity

Crashworthiness and impact mechanics are two principal terms in the field of crash and safety analysis. Therefore, the fundamental concepts of this area should be elaborated before designing of energy absorbers. Generally speaking, the application of energy absorbers is mainly associated with transportation industry and vehicles, which include variety of aircraft, and ground vehicles.

In the case of collision and impact condition, the structural component can have complicated behavior as the response of dynamic load. However, the design of energy absorbers was based on having a predictable crushing behavior which can translate the kinetic impact energy to dissipated irreversible energy.

1.2.1 Crashworthiness and structures

Generally, the crashworthiness term is defined as the capability of a vehicle body to be exposed to impact loads and protect the passengers, who are inside its survival space, from injuries or fatalities. Therefore, the area of structural crashworthiness is actually a study of the impact performance of a vehicle when collision occurs [1]. For many years, the focus of crashworthiness has been placed on the protecting of a vehicle's safe space. It can be observed that the capability of energy absorption system was evaluated by its capacity to absorb kinetic energy and maintain the safe space during a crash event, Figure 1-1.

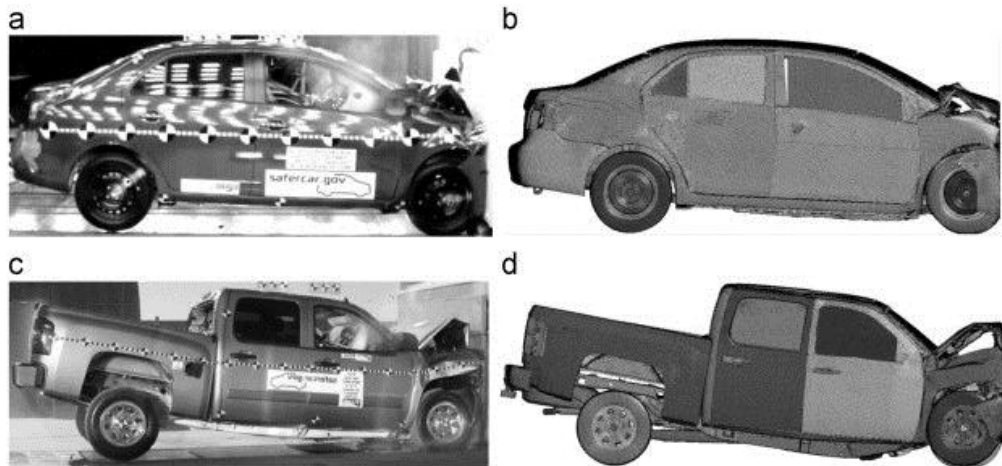


Figure 1-1 Comparison of vehicle deformations from the NCAP frontal crash tests of; (a) Yaris and (c) Silverado, with the numerical models (b, d) [2]

From the basic point of view of crashworthiness design, a dynamic load translated to the vehicle structural body must be much lower than the threshold that can cause irreversible deformation of the safe space. If the performance of structure satisfies the crashworthiness requirement, the absorber can be used as a protecting system for collision cases. Moreover, it is vital that the deformation of safe space to be minimal as well as the dynamic deceleration [3].

The main structure of an energy absorber device consists of thin-wall structures such as crash box. Attaching this component to the frame can provide safety during a collision. Figure 1-2. illustrates a front crash box attached to the chassis. The crash boxes are changeable and after a collision, one can replace and attach a new crash box to the chassis. In the case of a crash, the energy absorber takes the load initially and deforms to dissipate the impact energy although transferring the load to the structure can cause bending and deformation of other parts. There are different types of energy absorber systems which will be discussed later, however, classically thin-walled tubular structures have been used in transportation industry for many years.

Generally speaking, a crashworthiness analysis includes various aspects about the capability of a vehicle to provide safety, the performance during and after collision, and the collapse properties of the structure.

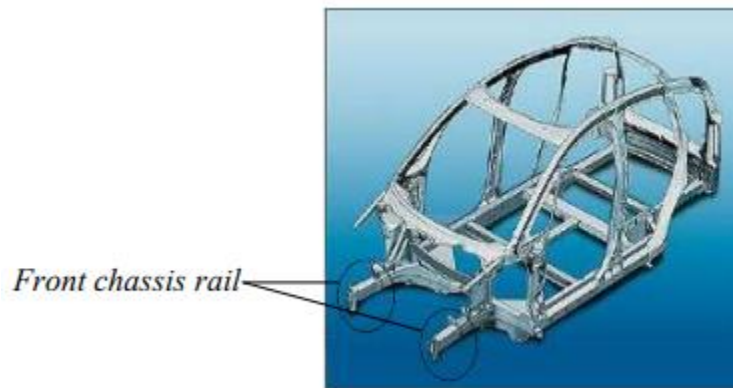


Figure 1-2 Front chassis rails as an energy absorbing device [4]

1.3 Energy absorption by irreversible deformation

The design of crush energy absorbers should consider a predictable collapse behavior and a controlled reaction force. The crashworthiness properties of thin-walled tubular

structures can be tuned in many ways to satisfy their application requirements. There are plenty of criteria to be considered to determine the efficiency of energy absorbers. In this section we will be covering the critical parameters for designing a crushing energy absorber.

1.3.1 Properties of energy absorber device

Basically, the overall performance of energy absorbers can be obtained by studying their load-displacement response during the collision event. The total absorbed energy E_a is defined as the total area under the load-displacement diagram.

$$E_a = \int_0^{\sigma_{max}} P \delta d\delta \quad (1)$$

Where P is the incremental crushing load, δ is the related displacement in each increment. From Equation (1), the mean crushing load can be calculated using the following equation.

$$P_m = \frac{1}{\delta} \int_0^{\sigma} P \delta d\delta \quad (2)$$

Generally, the collapse load is defined as the required force to initiate permanent deformation, which can be propagated in the collision event. Ideally, the energy absorber device can provide a constant crushing force, P_{max} from the onset of the deformation up to the maximum crushing displacement, σ_{max} . As mentioned before, the total energy absorption can be calculated by computing the area under load-displacement diagram. Figure 1-3 illustrate a simple depiction of an ideal energy absorber.

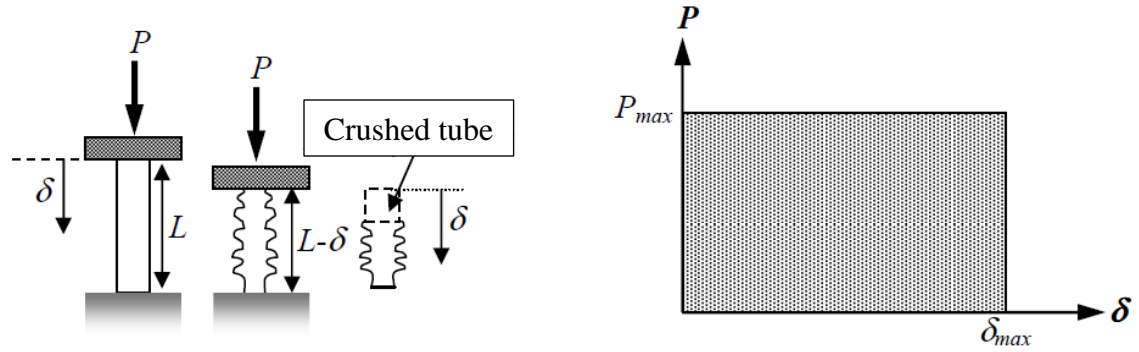


Figure 1-3 An ideal energy absorber and its response under crushing load [5]

1.3.1.1 Specific absorbed Energy (SAE)

When it's come to the efficiency of an energy absorber, one of the most critical characteristics is the ability to absorb energy per unit of mass. This characteristic is called specific absorbed energy (SAE).

$$SAE = \frac{E_{abs}}{m} \quad (3)$$

The importance of this parameter is to detect a lightweight energy absorber with the ability to absorb the required crushing energy [6]. Using different materials and techniques can alter this parameter. Foam-filling of hollow structures and multi-cell tubular absorbers should be designed in order to have a high SAE value.

1.3.1.2 Mean Crush load

The mean crushing force or load in here is shown by P_{mean} which is defined by dividing the total absorbed energy by the crushing displacement, δ .

$$P_{mean} = \frac{E_t}{\delta} \quad (4)$$

This parameter indicates the capability of device to absorb crushing energy when the crushing displacements is in comparison. Due to the nature of crushing, the thin-walled tubular absorbers present a fluctuation of crushing load in the plateau region, Figure 1-4. At the beginning of the crushing the reaction force increases sharply to reaches the highest value (P_{peak}) which then followed by a progressive crushing of the absorber. This parameter shows the initial rigidity against crushing load.

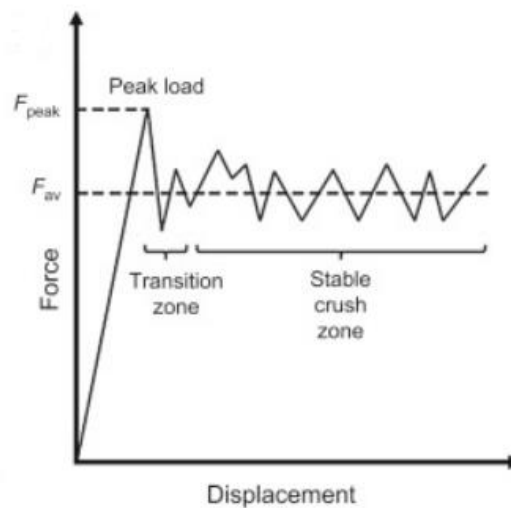


Figure 1-4 Typical load-displacement diagram for a thin-walled tubular energy absorber under axial crushing load [7]

1.3.1.3 Stroke efficiency

One of the important crashworthy parameters is the deformation length of energy absorber during the impact. Therefore, the required crushing energy to be dissipated per unit of length can be determined. This parameter is defined by dividing the maximum allowable crush distance by the initial length of the energy absorber. Due to the nature of crushing and densification of the deformed absorber this parameter is less than unity.

1.4 Types of crushing energy absorbers

After realizing the importance of kinetic energy dissipation during a collision, various types of crushing energy absorbers have been suggested over time. The basic idea among all those devices is the same which is consume the impact energy in an irreversible way such as plastic behavior or fracture. There are effective parameters that can distinguish the energy absorbing systems such as cost, weight, ease of assembly, and replacement. In this section different types of energy absorbing systems are discussed as follows:

- Metallic thin-walled structures
- Foam structures
- Reinforced structures

1.4.1 Metallic thin-walled structures

Thin-walled tubes are the most popular type of energy absorbing systems. These structures are in use in many structural applications. The idea behind their design is to provide a controllable crushing mechanism and progressively convert the kinetic energy to dissipated plastic energy [8].

Needless to say that the material properties and the structural geometry are the two influential parameters in energy absorption capacity of the device [9]. In terms of structural geometry there are many different thin-walled cross-sections such as circular, square, rectangular, and honeycombs that drawn the attention of researchers in this field. In the following sub-section, we will review some of the most common cross-sections for designing energy absorbers.

1.4.1.1 Circular cross-section

These tubes have proven themselves as an efficient structure against axial crushing events. The device can be designed with various foil thicknesses and circular diameter to satisfy the required energy absorption capacity [10]. Investigation on circular tubes goes back many years ago when numerous papers have been studied the performance of these structures [11-15]. The conventional studies were mainly experimental lab works; however, some analytical formulations have been developed to anticipate the crushing response of tubes based on a repetitive folding deformation, Figure 1-5.

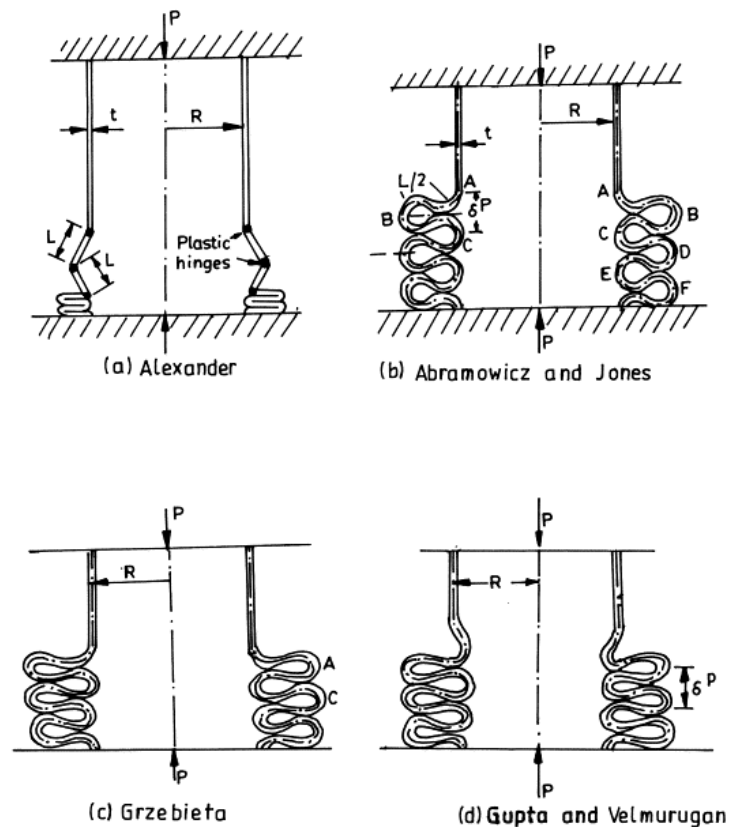


Figure 1-5 Models of axisymmetric deformation in concertina mode [2]

Afterwards, due to the advancement of computational analysis, more studies used finite element modeling to study the crashworthiness of these structures.

The crushing behavior of circular tubes has been observed as a stable collapse from which the deform shapes are known as axisymmetrical ring [13], non-axisymmetric (diamond mode) or mixed mode [15], Figure 1-6.

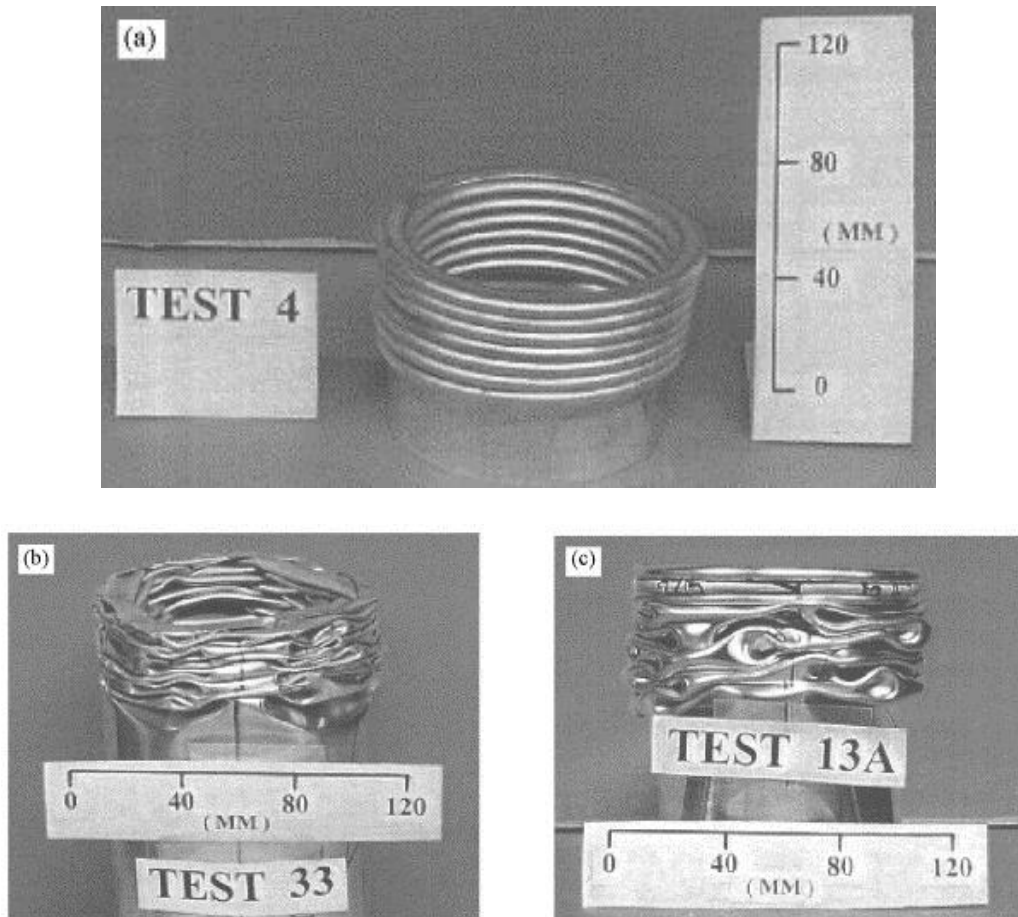


Figure 1-6 (a) axisymmetric mode; (b) non-symmetric mode; (c) mixed mode of axial crushing [14]

The mode of crushing is dependent to the ratio of diameter to thickness (D/t), the ratio of length to diameter (L/D), and the material properties of the tube. Generally speaking, thicker circular tubes intend to deform under axisymmetric mode, but thinner tubes deform in a non-symmetrical mode. The mixed mode deformation can be defined in a place where a transition from axisymmetric to non-symmetrical modes tends to happen. The biggest

challenge with the crushing response of the circular tubes was the high value of maximum load just before the progressive crushing response.

1.4.1.2 Rectangular crushing tubes

Another cross section of thin walled absorber is rectangular cross sections with perpendicular walls. The response and performance of these tubes have been investigated since 1984 [12] which then followed by more in-depth works on the behavior of these structures under static and dynamic loading conditions [16-18]. Although there are similarities between the crushing load-displacement diagram of rectangular tubes with circular ones, their deformation modes are different. Jensen et al. [19] reported that rectangular tubes have high variation of crushing load during collision.

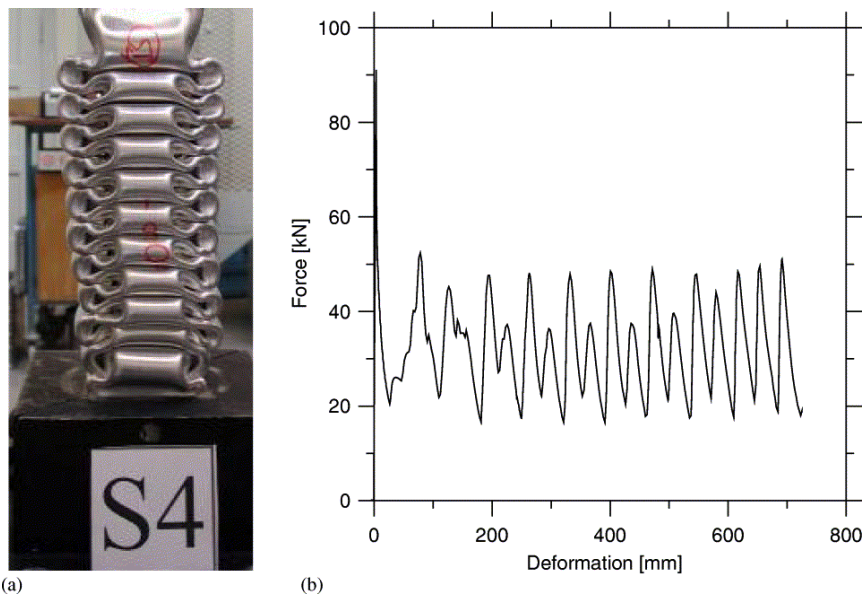


Figure 1-7 (a) Deformation mode and (b) force–deformation curve of a rectangular tube under axial crushing load [19] Moreover, the geometry of these structures must be meticulously controlled such as initial length, cross section dimensions, and thickness, as these tubes tend to deform under global bending condition which is counted as an unstable crushing mode [20]. Global bending of

a tubular structure a significantly decrease its capability in energy absorption. One way to prevent global bending and buckling of the tube was to provide a triggering mechanism (chamfer/tapered) at the end of square tubes to guide and control the beginning of wrinkling [21].

Comparing with circular tubes, it has been reported that the actual static crushing load is smaller for a square tube with the same foil thickness and solidity ratio (A/A_t). Hence, the effectiveness of square tubes is lower than circular counterparts. Due to this reason, circular tubes have been more preferable in terms of axial crushing energy absorption [12]. However, in a real impact situation, the crushing load might not be perfectly axial, and the absorber exposes oblique crushing loads. Despite this fact, only a few investigations on the oblique impact of the crushing absorbers have been conducted [22].

1.4.1.3 Conical tubes

Another type of energy absorber that has been implemented in different industries is conical tubes. They have a pretty stable response and relatively high energy absorption capacity [23]. The related investigations on these structures can be classified into numerical and experimental studies [24, 25]. It was reported that occurrence of global buckling during crushing is less probable for conical tube absorber compared with its cylindrical counterpart [26]. Therefore, it has more stable crushing response and preferable since it provides a larger Euler buckling load. Due to the inclined walls and the angle with respect to the tube axis, conical tubes do not need a triggering mechanism as is required for a circular tube [27]. The crushing properties of conical tubes is related to the mentioned features before and also the cone angle [28], Figure 1-8.

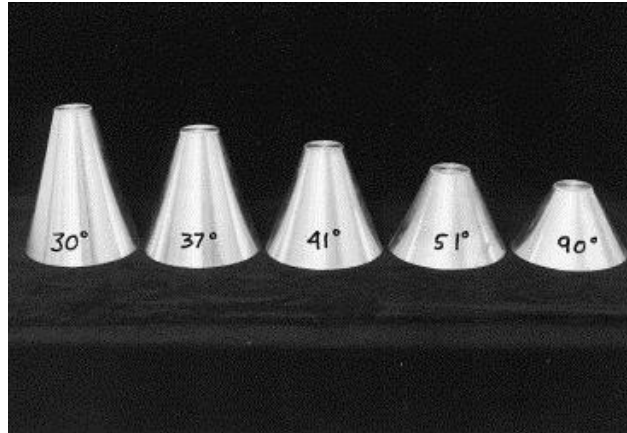


Figure 1-8 conical crush energy absorbers with different cone angles [28]

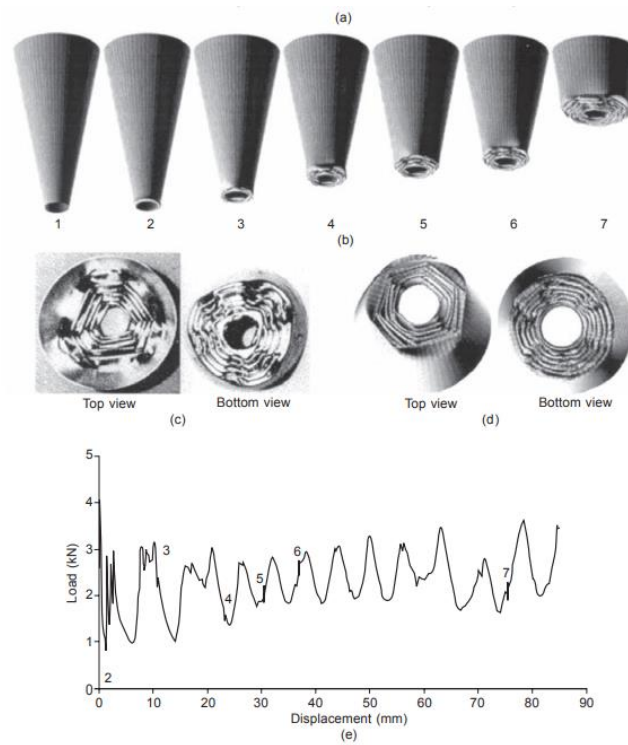


Figure 1-9 Crushing response of the conical tube [29]

Figure 1-9 shows the crushing response of a conical tube under axial loading. It can be seen the crushing occurs in a repetitive manner in axial direction. However, the crushing response has a large initial maximum load and significant fluctuations during crushing process.

1.4.2 Polymeric and Metallic Foams

In addition to the metallic structures that are being in use as energy absorbers, polymeric foams are another alternative. Polymeric foams can be classified into two types of closed-cell and opened-cell. Foams response under axial loading provides a smooth load-deflection diagram Figure 1-10, [5].

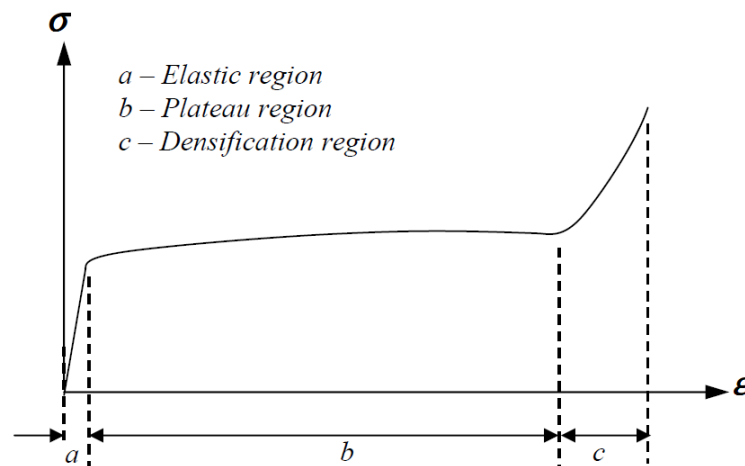


Figure 1-10 A typical nominal stress-strain curve for foam materials [5]

Due to their unique structure, foams can take large deflection and provide a steady low stress level during crushing [30]. According to a typical crushing response the first region of load-deflection is associated with linear elastic deformation, the second region which is comparatively large is the plateau crushing region, and the last region which has a sharp increase of crushing load is called densification region. Metallic foams are also popular as a lightweight crushing energy absorber. Among different materials, aluminum foams have drawn much attention due to its unique characteristics.

1.5 The target structural components

1.5.1 Longitudinal crash rails (front chassis rails)

The carbody of vehicle has a big portion of vehicle total mass (almost 20%) [31]. The carbody which is known as the skeleton of vehicle is the largest subassembly of the system. To meet the safety protocols, a carbody must be able to provide a safe cabin an acceptable crashworthiness property. The stiffness of carbody needs to be high enough to guarantee the integrity of structure against severe loading scenarios. On the other hand, the crush zone of the carbody is collapsible and deforms in a predictable way to absorb the impact crushing energies.

The most critical part in this zone is the longitudinal crash rails. It has been reported that in crash scenarios approximately 35 % of impacts are in the longitudinal direction (front) and this load should be mainly dissipated through the deformation of longitudinal crash rails. Aluminum tubes are the most common elements for manufacturing longitudinal crash rails. The previous studies illustrated that the thin-walled tubes present a high initial reaction force before the collapse progress and the reaction force fluctuates in the crushing zone due to the buckling of straight tube. Therefore, there are some researches about optimizing the performance of these tubes by introducing corrugations along the longitudinal direction. However, the corrugated tubes reduce the capacity of energy absorption as the tube is deformed easier [32].

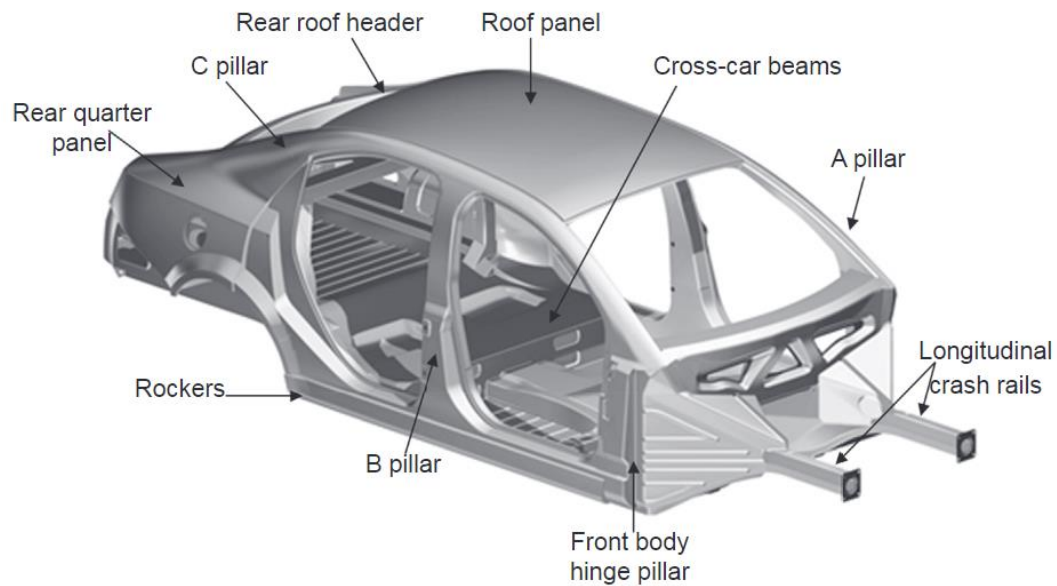


Figure 1-11 A brief overview of some key body structure elements [31]

1.5.2 Railway Axle

Railway axles are known as the most loaded parts in the railway vehicles since they account for about 70% of wagon mass. Axles are designed against endurance limit. While failures occur in axles because of very long fatigue life about 30 years and in-service damages. Defects from sub-surface and surface defects, predominantly initiating at corrosion pits [33] and nucleated micro cracks [34]. Fatigue crack initiation and corrosion pits mostly occur due to the flying ballast impacts [35]. The flying ballast is caused by a combination of mechanical forces such as falling ice blocks on the railway track, and aerodynamic forces. It is reported that 30 % of the major problem in terms of safety and early deterioration of the high-speed railways were due to flying ballast impacts [35]. The micro-cracks initiate from ballast impacts, typically small, sharp gravel particles or pebbles from the sleeper beds of railway tracks [36]. The cracks propagate as the stress state increased

and caused rupture in axles and catastrophic failures [37]. Flying ballast can affect the safety of staff working along the railway lines, train safety and consequently passenger or cause financial damage to the railway vehicle and the infrastructure maintenance [38]. Since, no regulation is defined by international standards about flying ballast, implementing a method to protect the vehicle axle will control the inflicted damages to the rolling stocks and decrease the maintenance costs.

One of the first solutions was provided by Murphy et al. by using a rubber layer on axles. The rubber had to be removed for inspection in an expensive operation [39]. The model was improved by Kontio et al. by altering the protective device to a circular-cylindrical pipe consist of an inner and outer layer which the inner layer was made of foamed plastic and glued to the outer layer. The whole system fastened to the axle. Therefore the installation process was faster than the previous method [40]. However, tight connection thereof against the axle lead to trapping moisture between the inner layer and the axle. The rusts created due to moisture might form cracks and axle damages. To remove this problem, an updated version of the previous model was proposed by Tolérus and Lundhammar by adding radial gaps and elongate ridges which formed an air channel between the cover and the axle [41]. A less expensive technique was proposed by Chretien et al. where the axle was protected by supple polymer strip with an easy assembly and disassembly process. The application of mentioned protective systems was limited to the axle classes which depends on the rolling stock speed. A protective system which could be implemented to rolling stock with independent of their class while facilitating different inspection of the axle were presented by Guenard and Thouvenot. The system consists of two or three layers of different materials. The first layer is capable of adhering to the axle, consist of aluminum

and elastomers on an adhesive compound. The second layer comprises at least one adhesive compound in pasty form of putty-like. Depending on the axle class, the third layer may be implanted. Moreover, using special adhesive and different layers of protection improve the shock absorbing properties [42]. However, the designed system could not protect the axle against the flying ballast. Therefore, the outer layer was substitute with a relatively hard shielding layer to resist against ballast impact without cracking and a flexible inner layer as a damper [43]. Another protection device was proposed by Dohn and Jensen to fulfill axle protection against flying ballast, grit and chunk of ice while preventing corrosion. The protective device has a substantially tubular shape comprises a shell and spacers which creates a gap between the shell and the axle which acts as an anti-corrosion system. The gap and the rotation of the wheel lead drainage of the condensed water. The device can be easily removed for a safer maintenance and inspection. A two half shells protective device were also presented by adding elastomer strips. Based on the axle diameter, different elastomer thickness can be implemented since the elastomers are interchangeable. Accordingly, the manufacturing costs for making shells with different diameter will be eliminated. Besides, the number of strips can be varied and optimized to reduce the cost as well [44]. However, the protective devices might not be practical from exposure to climate factors. The considerable change in the elastic properties of the layer and gap size could affect the reliability of the device. Additionally, the designed devices do not cover the entire wheelset and these areas can be exposed with external agents and result in serious structural failures. To solve this issue, a protective covering technique were applied to the at least metal surface of the wheelset. It consists of three painting layers, the first layers promoting the adhering properties. The second layer provide an elastic support for the

stiffer layer which protect the axle and wheelset against ballast impacts. The second and third layer are epoxy-based paint which enforced with fiber [45]. Although the protective layers are not subjected to softening at higher temperature, the inspection may become a problem. Also, the maintenance will be more laborious and expensive since the coating has to be repaired locally.

Chapter 2: Double sided composite corrugated tube

2.1 Introduction

The development and validation of the finite element model (FEM) for the corrugated tube under axial loading is explained in this chapter. Validation of the corrugated tube has been done by comparing the results of finite element simulations against the available analytical solution. The validated model then can be used for further studies for different geometries, material properties and various loading conditions.

2.2 Development of the FE model for thin-walled tubes

Nominal tube dimensions were adopted at 112 mm in length, 80 mm in diameter and 1 mm in thickness [46], regardless of detailed shape configurations, as shown in Figure 2-1. Corrugations were considered to be in sinusoidal form with corrugation length λ_c and corrugation amplitude a . Since the tube was fully corrugated with 14 corrugations along the tube length, SSC, DSC or DSC-C tubes were also referred to as SSC-14, DSC-14, or DSC-14-C respectively.

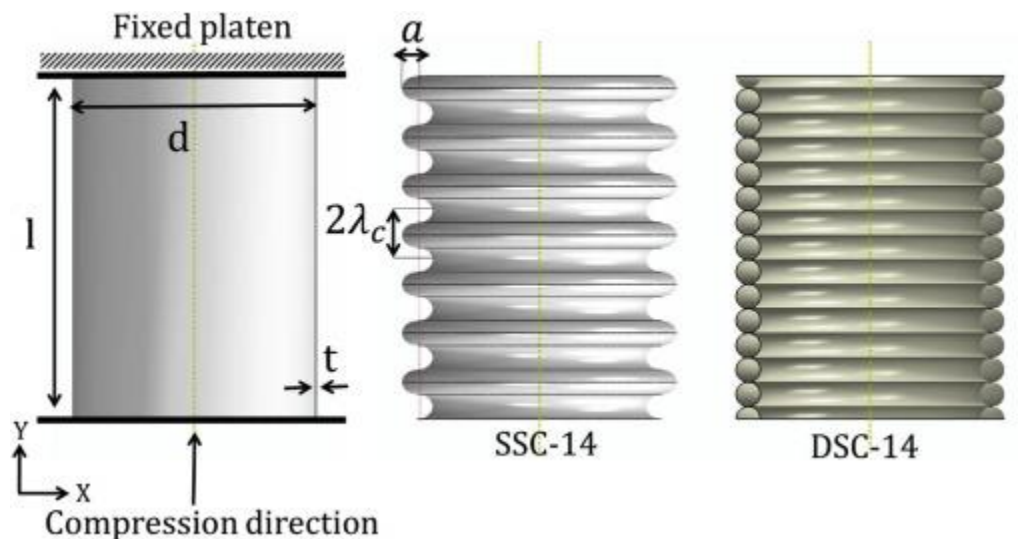


Figure 2-1 Three-dimensional tube configurations. Left, Straight tube with constrains; Middle, single-sided corrugated tube with corrugation parameters; Right, double-sided corrugated tube.

Both ends of the tube were confined by two rigid plates. The top plate was fixed and the bottom one allowed the Y-direction translation only, with a displacement rate of 5 mm/min. The general frictionless node-to-surface contact was prescribed between the rigid plates and the tube. All tubes, except the composite one, were made of Al 6060-T6 aluminum alloy with Young's modulus of 71 GPa, Poisson's ratio of 0.33, density of 2700 kg/m³, yield strength of 160 MPa, and ultimate tensile strength of 200 MPa. The elasto-plastic constitutive material model was adopted. For the composite DSC-14-C tube, CF1263 carbon/epoxy composite layup was chosen [47] with materials properties listed in Table 2-1.

Table 2-1 Mechanical properties of laminate composite material CF1263.

| Density (kg/m ³) | Elastic modulus (GPa) | | | Shear modulus (GPa) | | | Poisson's ratio | | | Tensile strength (MPa) | | Compressive strength (MPa) | |
|---------------------------------|--------------------------|-------|-------|------------------------|----------|----------|-----------------|------------|------------|------------------------------|------|-------------------------------|------|
| | E_x | E_y | E_z | G_{xy} | G_{yz} | G_{xz} | ν_{xy} | ν_{yz} | ν_{xz} | Fill | Wrap | Fill | Wrap |
| 1520 | 58.36 | 48.42 | 10.66 | 5.84 | 3.65 | 3.65 | 0.12 | 0.45 | 0.45 | 885 | 1018 | 513 | 542 |

The Hashin progressive damage model [5] was adopted and the damage is determined at the point when each of several damage criteria was met. Each damage criteria compares the calculated stresses against the strength properties of the respective material. Energy-based damage evolution was employed to encompass strain softening response of CFRP composite. The stacking sequence of the composite tube was [± 45 degrees] with the thickness of each layer at 0.25 mm. The laminate had four layers and a thickness of 1 mm in total. All tubes were meshed using S4R linear shell elements with five integration points. The shell element provides accurate modeling without greatly increasing the computational

time needed for each run. Mesh convergence analysis were conducted (Figure 2-2) and the 1 mm element size was chosen.

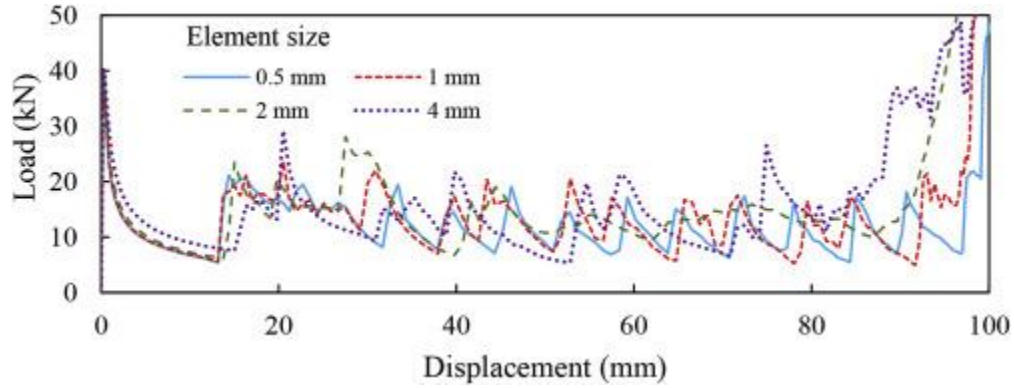


Figure 2-2 Load-displacement response of S tube for different element sizes

2.3 Verification of FE model

The analytical solution for an S-tube based on the kinetic approach [49] was used to validate our FE model results. The average compressive force over the whole crushing process could be calculated by [6]

$$\lambda = 0.920\sqrt{2Rt} \quad (5)$$

$$\frac{P_{ave}}{M_o} = \frac{25.23\sqrt{2R/t + 11.9}}{0.86 - 0.568\sqrt{t/2R}} \quad (6)$$

Where $M_o = \frac{\sigma_o t^2}{4}$ is the fully plastic moment per unit length, σ_o is the energy equivalent flow stress which is estimated as the 0.2% of yield strength [13], and λ is the half-wavelength of the wrinkle. R and t are radius and thickness of tube, respectively.

The average compressive force P_{ave} from our model was calculated by dividing the total absorbed energy, i.e., the area under the load-displacement diagram (Figure 2-3), by the displacement magnitude just before the densification point [46].

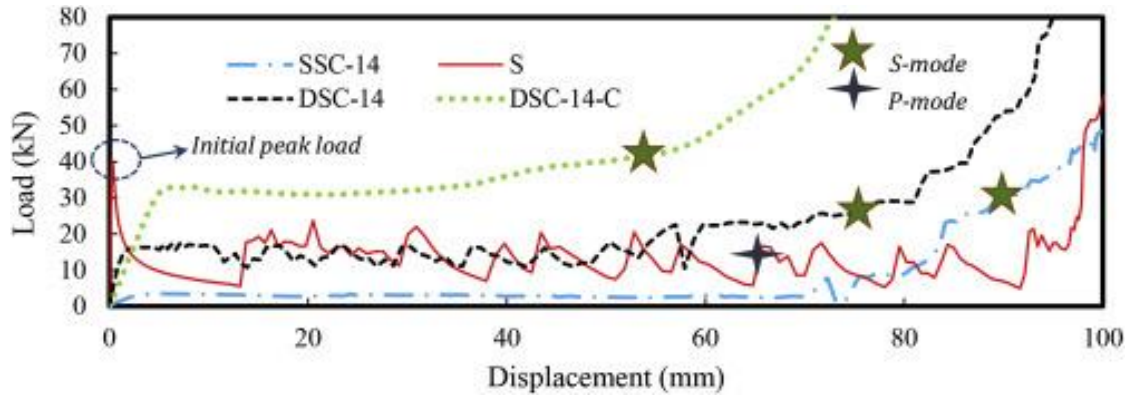


Figure 2-3 Load-displacement diagrams of the tubes under axial compressive loading.

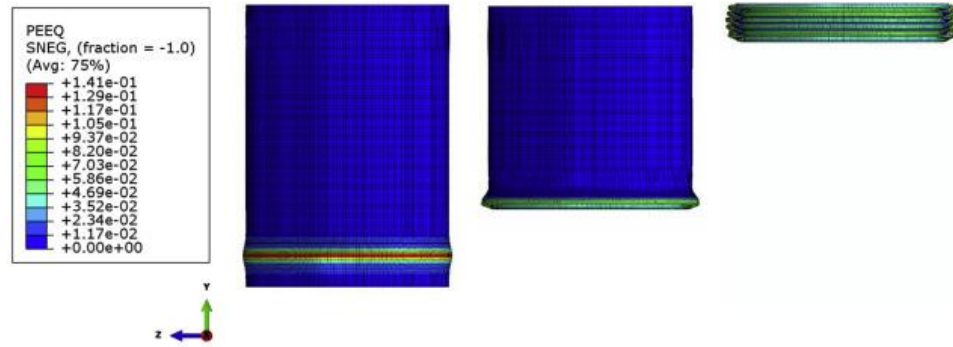
Moreover, λ was obtained by measuring the half-formed wrinkle length of the hinge. The calculated reaction force and the half-formed wrinkle length for the S-tube were 12.84 kN and 9.26 mm, respectively. The corresponding analytical results from Eqs. (5), (6) were 14.91 kN and 8.228 mm. The differences between the simulation and the analytical solutions were 16% and 12.5%, respectively. These variations could be explained by the assumptions used in the kinetic approach [48]. In addition, the modeling framework for composite materials was validated in our previous work [49], [50].

2.4 Mechanical performance of double-sided corrugated tube

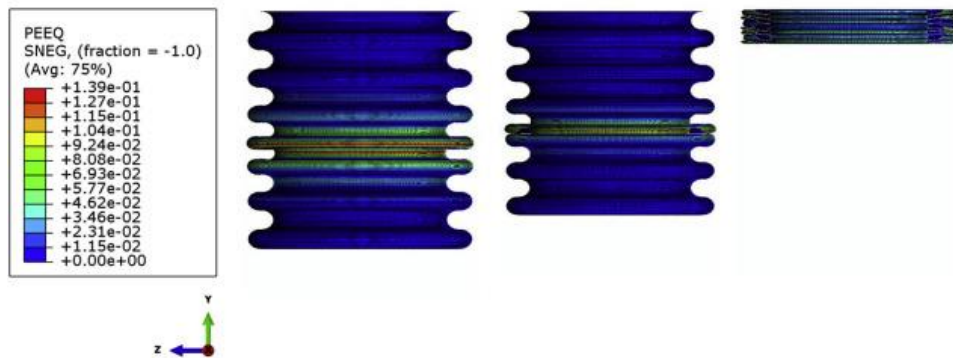
To improve the energy absorption capacity of the SSC without decreasing its controllable energy absorption of corrugation troughs, we tried a variety of corrugation shapes, such as moon shape, half-circular, diamond and half-diamond before finding the desirable DSC tube. The mechanical performance of the proposed DSC-14 tube was demonstrated by comparing it with existing tubes such as the SSC-14 and S-tube. Their load-displacement behaviors were depicted in Figure 2-3. It is clear that the DSC-14 could take more loads and thus absorb more crushing energy than both the SSC-14 and S-tube, especially at large displacement. The load fluctuation of the corrugated tubes was also relatively small

compared to the S-tube, which allowed better regulation of their energy absorption behaviors.

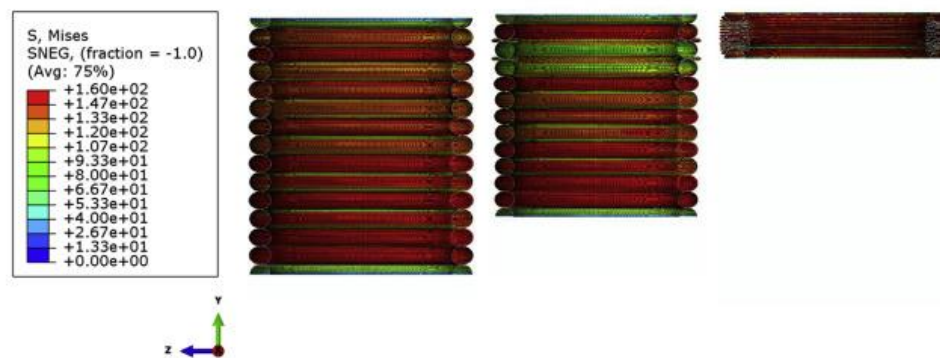
The advantage of the DSC-14 over the SSC-14 and S-tube could be visualized from the snapshots of tube compression, as shown in Figure 2-4. The contour plot of the equivalent plastic strain (PEEQ) in Figure 2-4 shows that the PEEQ concentrated around the folds, whose geometry parameters were the critical design factors for optimization of energy absorption ability. The percentage of DSC-14 tube surface with plastic deformation (PEEQ $\geq 0.1\%$) just before densification was 97%, while it was 68% for the SSC-14 tube, indicating a 170% relative increase. During the crushing of each corrugation, there are four plastic hinges for DSC-14 while there is only 1 plastic hinge for SSC-14 (Figure 2-5). Accumulation of these plastic hinges indicates the higher plastic deformation of DSC-14 compared with SSC-14.



(a) S Tube



(b) SSC-14 Tube



(c) DSC-14 Tube

Figure 2-4 Equivalent Plastic Strain (PEEQ) contours. (a) S tube: Left, first fold initiation at crushing displacement of 0.37 mm; Middle, second fold development at displacement of 31.75 mm; Right, final compressed state with crushing displacement of 97.83; (b) SSC-14 tube: Left, first fold initiation at crushing displacement of 17 mm; Middle, second fold development at displacement of 27.7 mm; Right, final compressed state with crushing displacement of 89 mm; (c) DSC-14 tube: Left, first fold initiation at crushing displacement of 11 mm; Middle, second fold development at displacement of 23.5 mm; Right, final compressed state at crushing displacement of 79.8 mm.

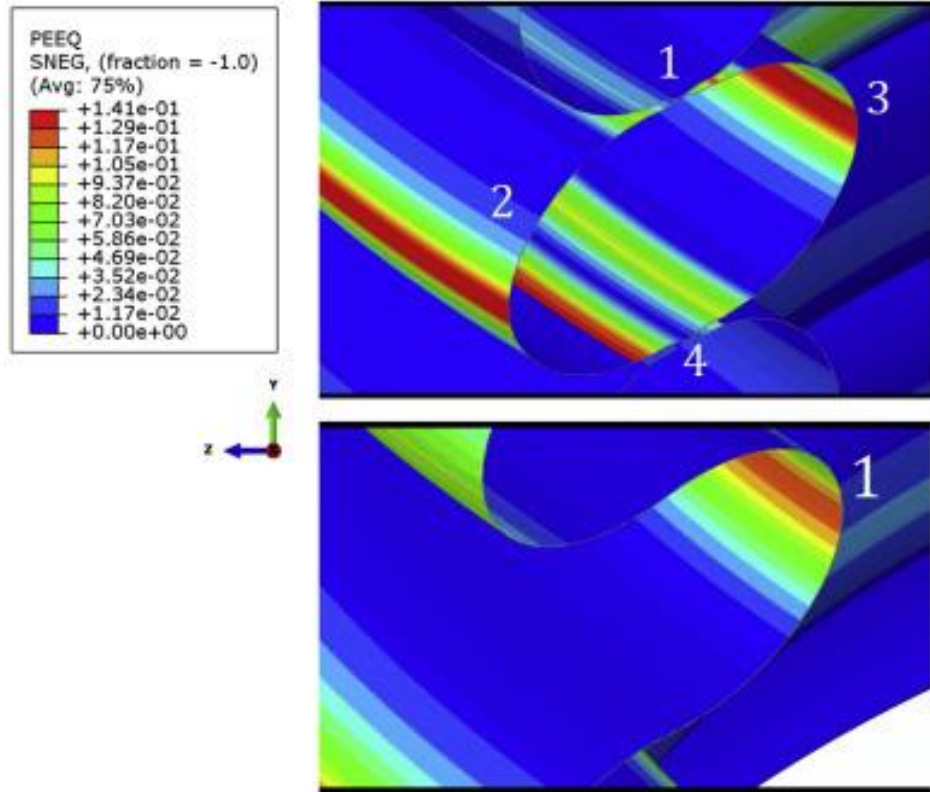


Figure 2-5 Folding schematics of DSC-14 (top) and SSC-14 (bottom).

The initiation of both first and second folds as well as the final compressed state were illustrated. For the S-tube, a single abrupt hinge was initiated near the crushing interface, i.e., the movable plate, when the plate displacement reached 0.37 mm. This first fold or hinge progressed until collapse (Figure 2-7), and then the new hinge was developed and so on. The PEEQ history at one specific point located within the formation of the first fold was plotted in Figure 2-6. The progression of the first fold from initiation to collapse resulted in the increase in the PEEQ and then stayed at a plateau.

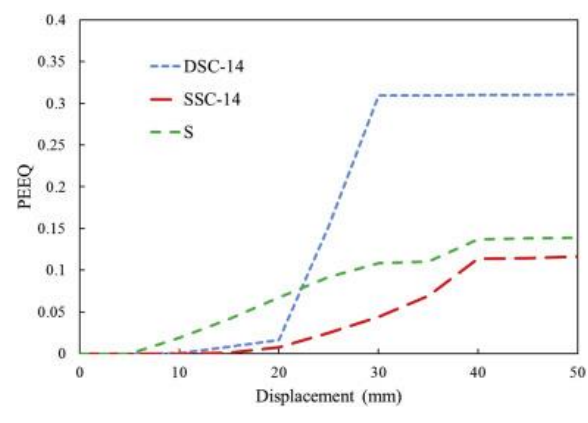


Figure 2-6 The (PEEQ) history at one specific region (first formed wrinkle) for S, SSC-14 and DSC-14 tubes.

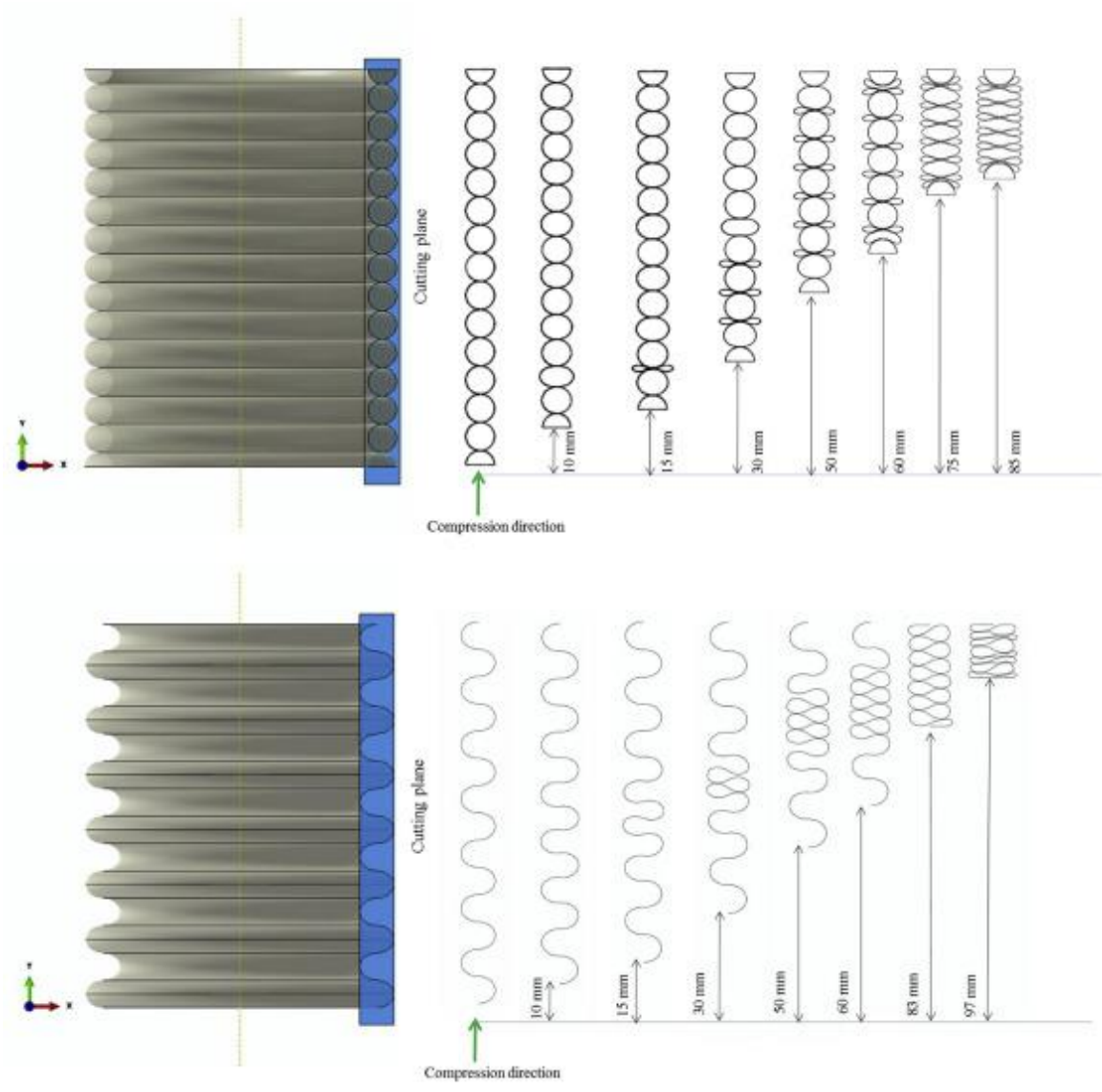


Figure 2-7 Crushing progression of DSC-14 (Top) and SSC-14 tube (Bottom).

The second fold initiated at a plate displacement of 31.8 mm, and the S-tube was completely crushed at a displacement of 97.8 mm. The location of the first fold agreed with the previous report [46]. In addition, the hinge collapse pattern led to a changing load fluctuation in the S-tube, also referred to as P-mode deformation, as labeled in Figure 2-3. This kind of axial behavior could be explained by the first hinge induced abrupt stress concentration, which resulted in the sharp rise in its load-displacement behavior and the plastic deformation regime.

The corrugated tubes exhibit a gradual increase in compression loading with a larger displacement, labeled as S-mode behaviors in Figure 2-3 and illustrated by the PEEQ contours in Figure 2-4 (b & c). The crushing load induced large irreversible plastic deformation, which determined the energy absorption capacity of the tubes. The first two folds initiated at a plate displacement of 17.0 mm and 27.7 mm for the SSC-14 tube, and 11.0 mm and 23.5 mm for the DSC-14 tube, respectively. The complete crushed state was reached at a plate displacement of 89.0 mm and 79.8 mm for the DSC-14 and the SSC-14, respectively. It is clear that the PEEQ region was located near the crushing interface for both DSC-14 and S-tube, but for the SSC-14, it initiated from the middle of the tube. The plastic hinge formation occurred more uniformly through the tube length. There was minimal fluctuation in the load-displacement response during crushing, which is associated with a reduced risk of injuries. This is a desirable characteristic in crashworthy design. It is also interesting to observe that the initiation of the first crushing fold for the corrugated tubes occurred relatively later than for the S-tube. However, it took much less crushing displacement, but more energy, to form the second fold in the DSC-14 tube in the than other two tubes. Besides, the final crushed state of the DSC-14 tube was relatively longer

than the other two. This indicates that the axial deformation of the DSC tube could play an important role in crashworthy design [32].

It is clear that the energy absorption capability of the SSC-14 tube subjected to axial crushing is notably lower than the S-tube with identical dimensions (Figure 2-3). This agrees with the work by Eyvazian et al. [32]. As expected, more crushing load could be absorbed in the S-tube due to the bending of a straight wall, resulting in more plastic bending energy. On the other hand, the load and dissipated energy was reduced in the SSC-14 due to the existence of radial corrugations [49]. This indicated that the formation of hinges in the S-tube demanded much more energy than guiding the deformation of single-sided corrugation troughs. For double-sided corrugations, the additional symmetric side reinforced the structural stiffness of the tube and thus altered the deformation pattern of the tube as illustrated in Figure 2-7.

At the compression displacement of 10 mm, the second corrugation near the crushing interface, i.e., the movable plate experienced relatively larger distortion and crushing before the initiation of the second plastic hinges, which was spaced in every other corrugation. This pattern of crushing behavior repeated until reaching the other end of the tube. Then the second level of crushing was initiated at the compression displacement of 60 mm. At this stage, the uncrushed corrugations underwent plastic deformation one by one. The corrugations underwent plastic folding along with the densification of the tube. Moreover, the double-sided corrugations were able to produce four plastic hinges at each corrugation, compared to only one plastic hinges for the SSC-14. This way, the tube resistance against crushing increased, resulting in a larger percentage of plastic zone and therefore a higher absorbed energy.

The crashworthiness parameters for each tube were characterized in Figure 2-8. Specifically, the average compressive force over the whole crushing process was 18.82, 4.38, and 12.84 kN for the DSC-14, SSC-14 and S-tube, respectively. The corresponding total absorbed energy, i.e., the area below the load-displacement curve, was 1.62, 0.38, and 1.22 kJ. The specific absorbed energy (SAE), defined as the total absorbed energy per unit mass, was calculated as 2.25, 0.97, and 5.55 kJ/kg for the DSC-14, SSC-14 and S-tube, respectively. Our proposed DSC-14 tube demonstrated a 32% greater increase in energy absorption than the S-tube with the same nominal dimensions. However, the SAE of the DSC-14 is approximately 40% of the one for the S-tube. To improve the SAE of the DSC-14, a composite tube, denoted as DSC-14-C, was then investigated.

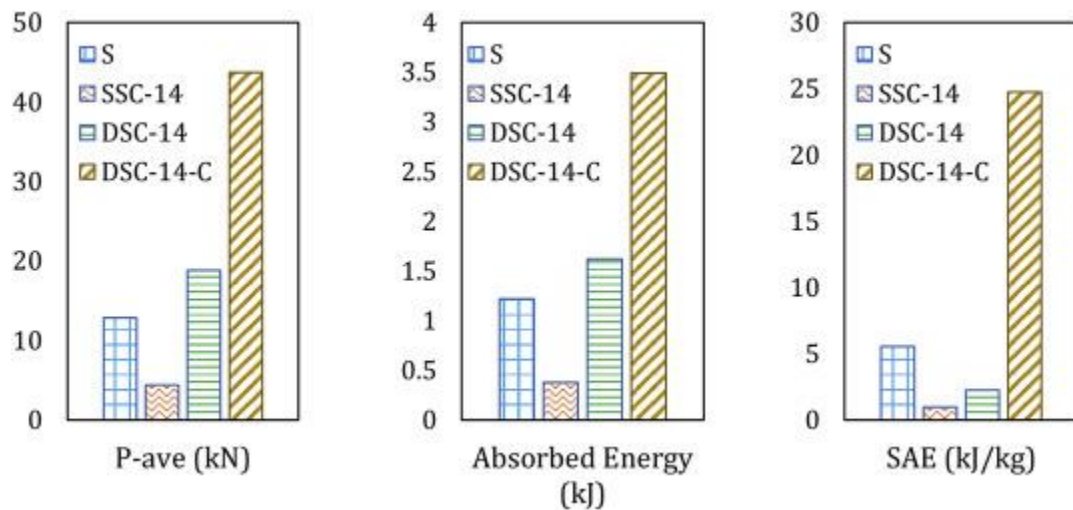


Figure 2-8 Crashworthiness properties of tube structures.

2.5 Composite DSC-14 tube

A dramatic increase in the load bearing capacity of the DSC-14-C was observed in comparison with the aforementioned tubes. The crashworthiness parameters for the DSC-

14-C tube were 43.71 kN for the average compressive force over the whole crushing process, 3.49 kJ for the total absorbed energy, and 24.75 kJ/kg for the SAE. The change of tube materials from Al 6060-T6 aluminum alloy to CF1263 carbon/epoxy composite laminate doubled the crashworthiness parameters in terms of the average compression force and the total absorbed energy and boosted the SAE by eleven times. The DSC-14-C had obvious crashworthiness advantages over the S-tube. The crushing progression of the DSC-14-C is similar to the DSC-14 as shown in Figure 2-4. The specific absorbed energy of the DSC-14 is 59% lower than that of the S-tube. The SAE value of the DSC-14-C is ten times higher than the DSC-14 and 346% larger than the simple straight tube, S-tube.

2.6 Effect of corrugation spacing on the performance of the DSC tube

The role of corrugation spacing on the crashworthiness of DSC tubes was also studied as shown in Figure 2-9. The nominal dimension of the tube remained the same. The number of corrugations for the aluminum alloy DSC tube was altered from 14 to 6 or 10, denoted as DSC-6 and DSC-10, respectively. As the number of corrugations increased from 6 up to 14, the corrugation spacing, i.e., the straight tube segment linking the corrugations shortened from 20 mm to 0 mm. Due to the corrugation spacing, relatively larger load fluctuations were observed in both the DSC-6 and the DSC-10, which were initiated at the crushing displacement of 49 mm and 79 mm, respectively. There is not any load fluctuation for fully corrugated DSC-14 tube. This indicated that the straight tube segment induced large load fluctuations during crushing, which might pose a safety threat to passengers, if any. Even though longer straight connectors resulting in a larger energy absorption, but less smooth crushing behavior is induced.

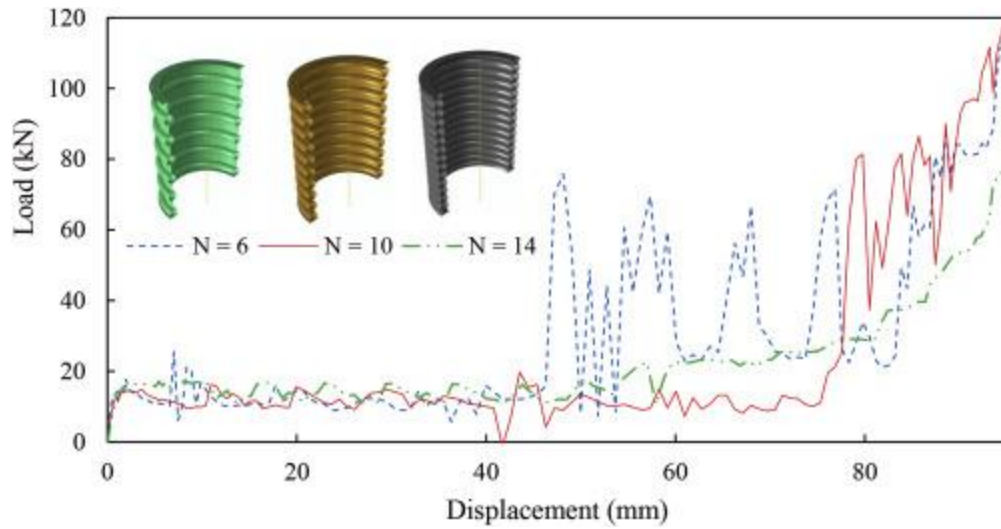


Figure 2-9 Corrugation spacing affect the crushing responses of DSC tubes.

The mechanism could be well demonstrated by the crushing progression of the DSC-6 tube (Figure 2-10). Prior to the compression displacement of 40 mm, the corrugations were plastically hinged one by one from the interface until reaching the other end of the tube, which correlated with the small fluctuations of load between 11 kN and 14 kN in Figure 2-10. At the compression displacement of 49 mm, the first large load fluctuation between 14 kN and 75 kN was observed corresponding to the plastic buckling of straight wall segments. Similar behavior happened for the DSC-10.

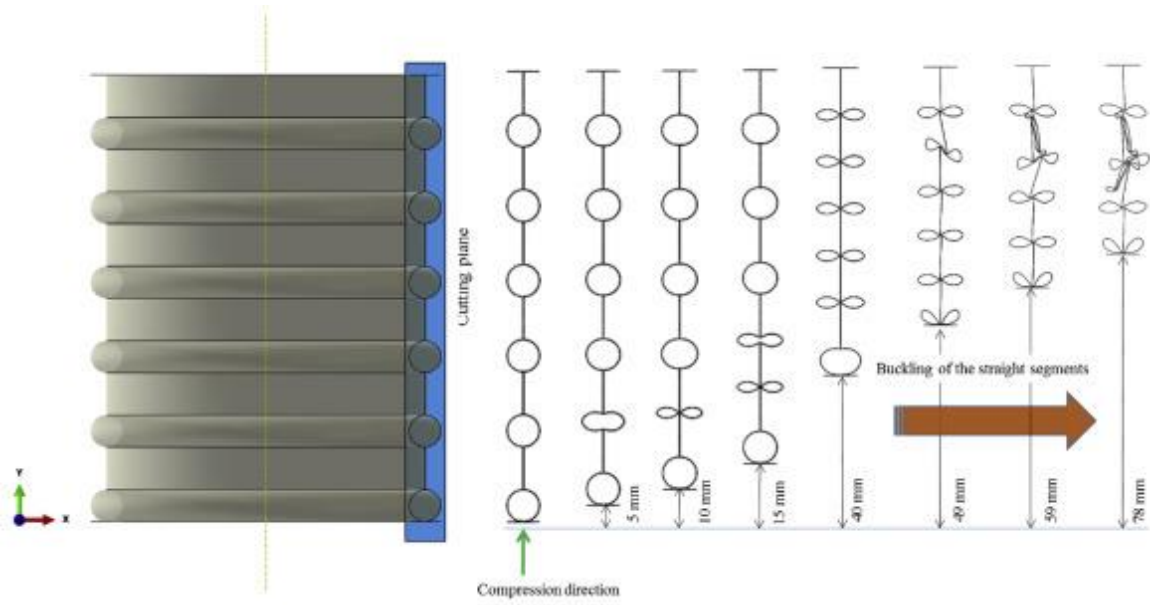


Figure 2-10 Crushing progression of DSC-6 tube.

Conventional single-sided corrugated aluminum tubes have demonstrated a desirable smooth load-displacement behavior, but at the cost of a lower energy absorption capacity, compared with the straight tube. In this work, we proposed and tested a DSC tube made of aluminum alloy or CF1263 carbon/epoxy composite. The aim was to improve the energy absorption capacity as well as preserve the controllable smooth crushing behavior, which is negatively associated with the safety threat to passengers. Finite element models were developed to test the new tube design following its validation against analytical solutions.

Chapter 3: Ballast impact protection mechanism

3.1 Introduction

This chapter is about the second part of the thesis. In here we are going to elaborate on the developed ballast impact protection mechanism. The design started with material searching to find an appropriate combination to design the sandwich panel for this application. Furthermore, a finite element model has been developed to incorporate the structural characteristics and mechanical properties of the suggested sandwich panel. According to the results of simulations, our team prepared the samples of sandwich panel to conduct out of plane impact tests. Finally, by comparing the results, we suggested the sandwich panel design for ballast impact protection mechanism.

3.2 Sandwich panel

Sandwich panels have been among top engineering materials in transportation engineering. Compared to the traditional metal sheets or composite laminates, the sandwich structures have considerable characteristics such as high energy absorption capacity, high flexural stiffness and strength. Basically, a sandwich panel consists of a low-density core and the stiff skins. The structure usually absorbs and dissipate impact energy by using two different mechanisms, namely, local crushing and global bending. For the ballast impact protection device, the first mechanism is more important as the sandwich panel is fixed on the axle. In the local crushing mode, the lightweight core crushed largely to absorb significant amount of impact energy. Therefore, the core material must be lightweight with an acceptable crush energy absorption capacity. The skin on the other hand, is responsible to provide bonding and integrity of structure. Here we have elaborated the materials of the ballast impact protection device.

3.2.1 Core material

The common and lightweight cores have open-cell or closed-cell structures such as Polyurethane and metal foams [51]. These materials have unique mechanical properties which make them interesting for a variety of structural applications. Among the different available polymeric and metal foams our team chose aluminum foams. These materials have interesting combinations of properties such as high stiffness, strength combined with high energy absorption capacity, and formability. These features guide us to choose these foams as the potential elements of the ballast impact absorber. Three aluminum foams were produced with different densities. Large foam cylinder was foamed and processed as cubic specimens ($25\text{ mm} \times 25\text{ mm} \times 25\text{ mm}$). In order to prevent any damage to the cellular structure, the cubic foam samples were cut by Electric Discharge Machining (EDM). Compression tests were performed (properties were determined) according to ISO 13314-2011.

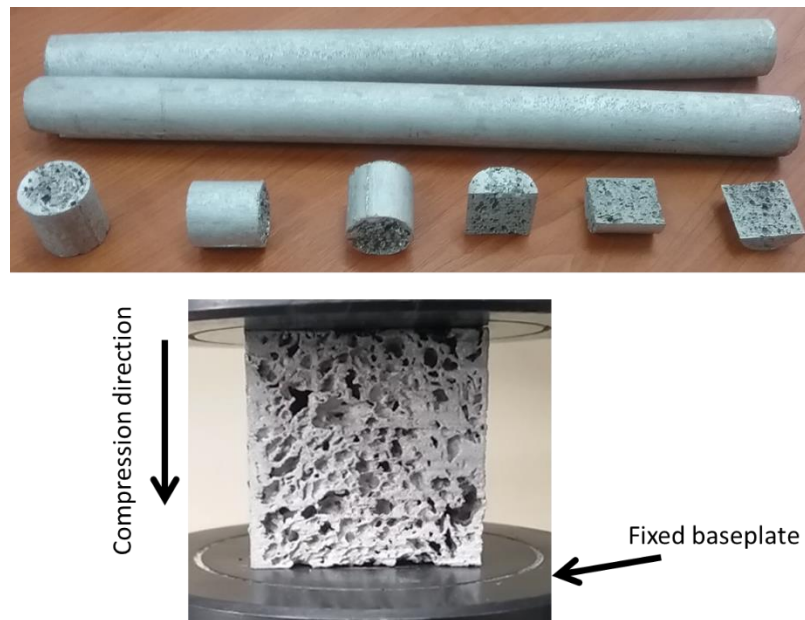


Figure 3-1 The prepared aluminum samples for quasi-static compression tests

The mechanical response of the foams was obtained by using quasi-static compression tests. For each case 3-5 tests were performed, and the average response was considered.

The naming of samples was based on their density.

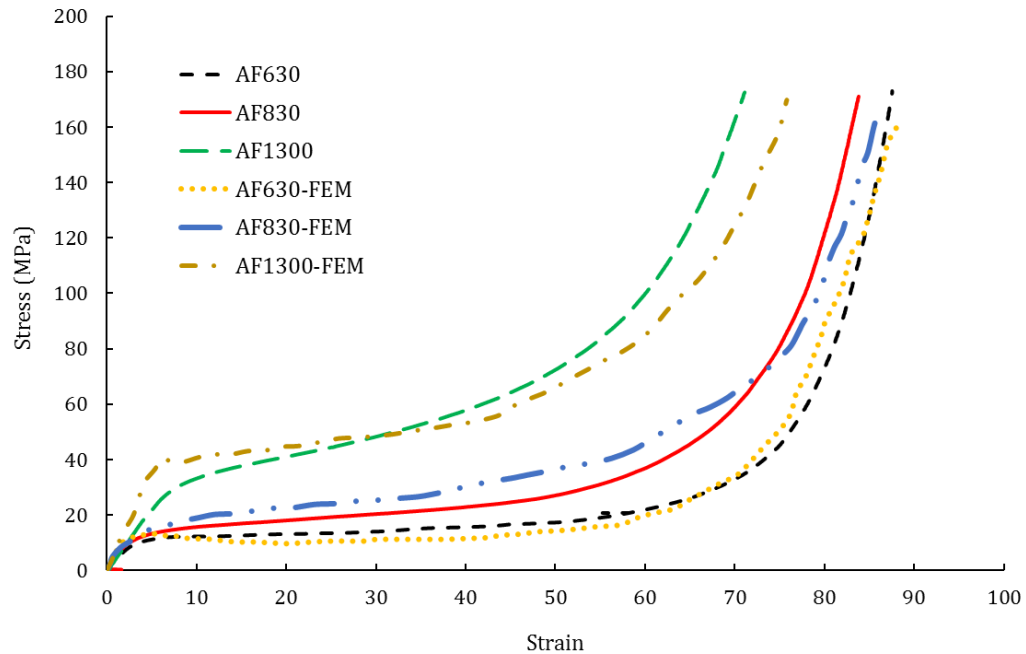


Figure 3-2 The stress-strain diagram of aluminum foam cores

Figure 3-2 shows the stress-strain curved captured during the compression tests for each foam. The mechanical properties of the foams are listed in Table 3-1.

Table 3-1 The mechanical properties of tested foams in preliminary stage

| Foam type | Density (kg/m ³) | Young's modulus | Poisson's ratio | Yield Strength (MPa) |
|---------------|------------------------------|-----------------|-----------------|----------------------|
| AF630 | 630 | 337 | 0 | 12.181 |
| AF830 | 830 | 402 | 0 | 13.1 |
| AF1300 | 1300 | 450 | 0 | 32.686 |

3.2.2 Skin material

Among the available materials such as mat, GFRP, CFRP and different metallic sheets, our team decided to choose aluminum alloy 6082 for the skin of sandwich panel due to its crushing performance, low cost, and good formability, Figure 3-3. The samples were made by Dr. Gabriella Epasto from University of Messina, Italy.



Figure 3-3 The aluminum sheets for preparing the sandwich panel skin

The mechanical properties of aluminum skin are described in Table 3-2.

Table 3-2 Mechanical properties of Aluminum alloy 6082 [52]

| Density | Young's modulus | Yield's Strength | Elongation at break |
|---------|-----------------|------------------|---------------------|
|---------|-----------------|------------------|---------------------|

| (kg/m ³) | (MPa) | (MPa) | |
|----------------------|-------|-------|------|
| 2700 | 70000 | 255 | 10 % |

3.3 Finite Element Simulation

3.3.1 Modeling

After choosing the constituents of the sandwich panel we needed to decide the dimension of sandwich panel. The most important parameter was the total thickness of the absorber which according to the Railway tolerance standard must be less than 50 mm, [39]. At the next step, the impact of flying ballast is simulated. According to NF F07-101 standard to describe the impact for simulating ballast projectiles, we used the K4 class corresponding to an impact with energy of 35 J. Due to the local effect of ballast impact, we used two cutting planes to take a section of axle and then applied symmetrical boundary conditions at both ends, Figure 3-4. The dimensions of the axle were obtained from [53]. The total thickness of absorber was 50 mm and the thickness of skin was 2.5 mm. The total number of nodes was 167925 and the total number of elements were 164220 which included 13000 linear quadrilateral S4R and 151220 linear hexahedral C3D8R elements.

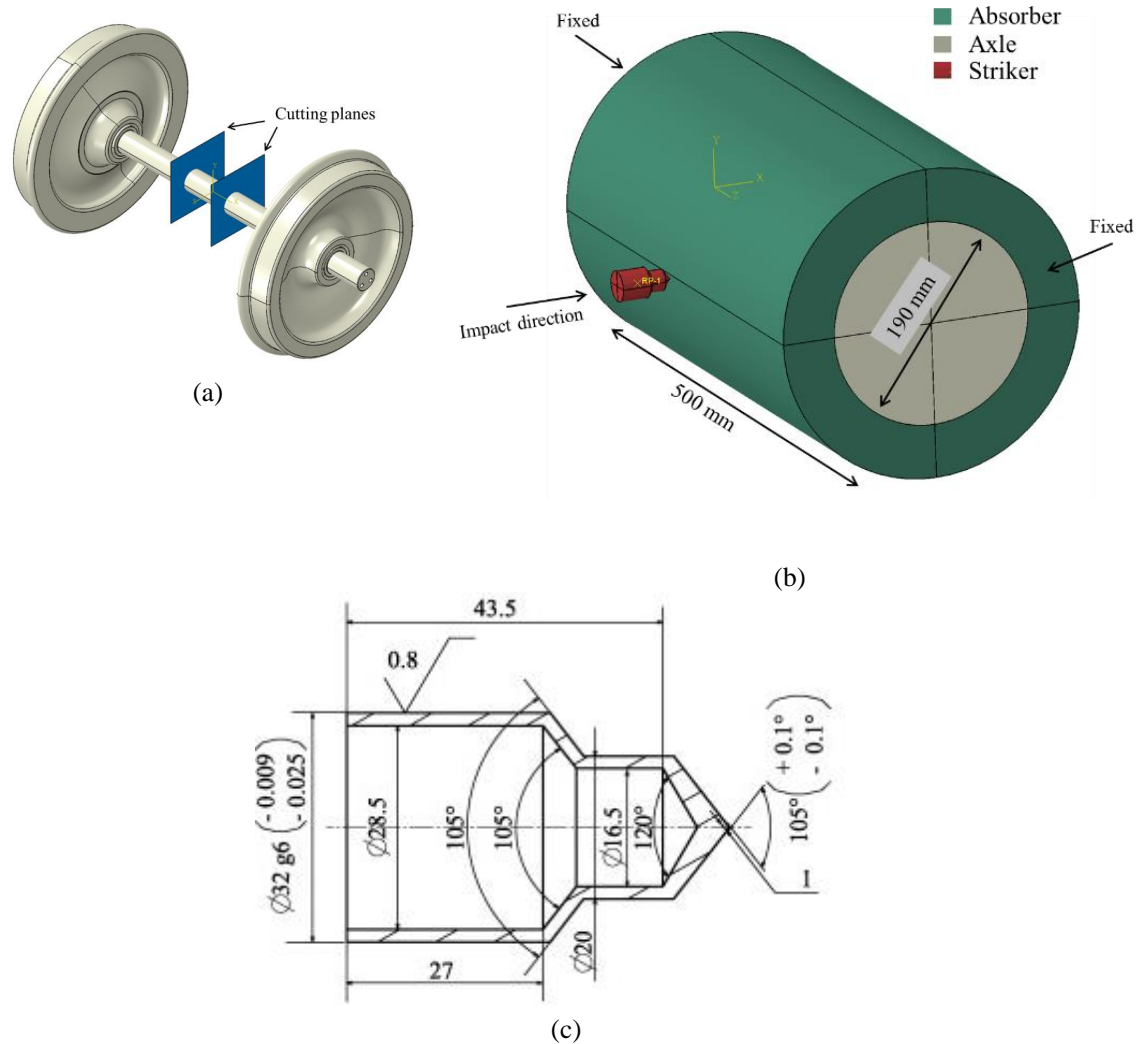


Figure 3-4 Finite element model of the impact analysis; (a) Railway axle model and the cutting planes; (b) the selected section of the axle covered with absorber; (c) The dimension of striker (mm).

The both ends of axle was constrained in all degrees of freedom. The striker was modeled by using rigid body feature and the point mass applied to its centroid. The magnitude of velocity was adjusted to provide kinetic energy of 35J. The axle was modeled as elastic perfectly plastic material. The model was meshed with 3D solid elements, Figure 3-5. The impact region was meshed with more refined mesh for the sake of accuracy and mesh sensitivity analysis were performed to obtain the optimum element size. Surface to surface

contact was applied between the striker and the absorber. The tie constraint was applied between the absorber and axle to simulate clamping mechanism. Moreover, an impact test was performed on the bare axle to observe the possible damage of the projectile on axle surface.

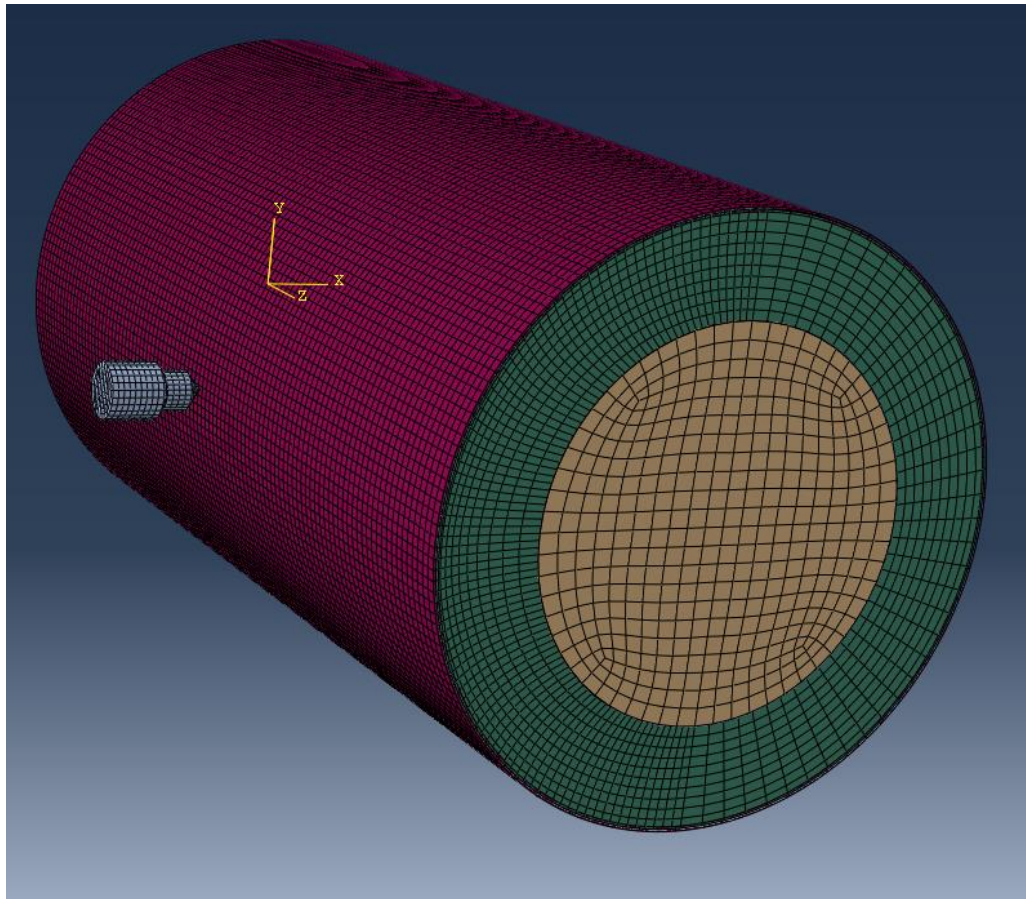
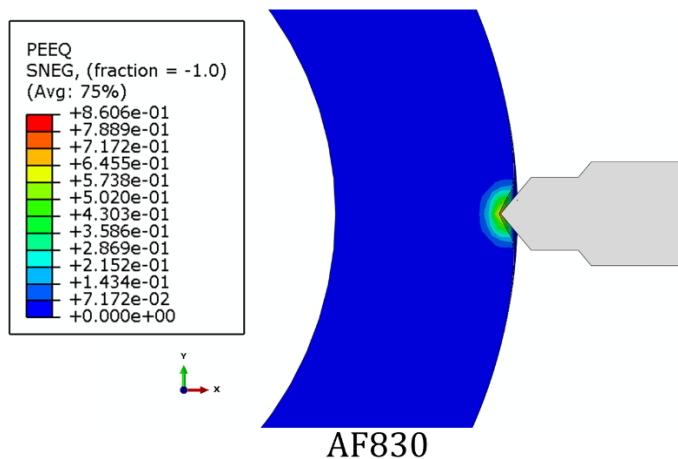
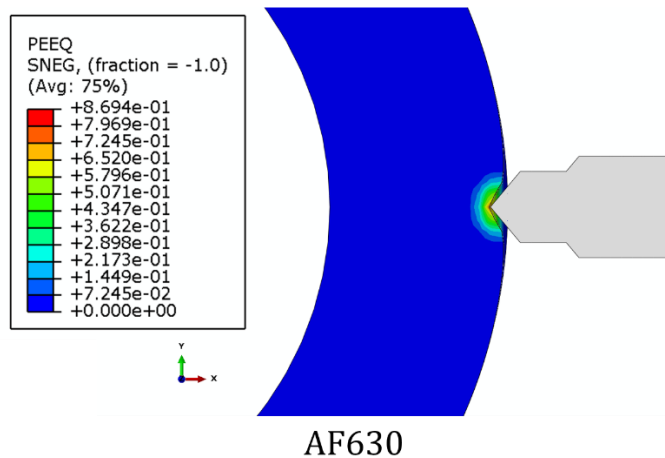


Figure 3-5 The meshed model of axle and absorber

3.3.2 Results

One of the critical parameters is the plastic deformation. This parameter shows that the permanent indentation and the irreversible deformation induced by projectile impact. Fortunately, in none of the cases we observed fully plastic deformation. In other words, a portion of deformation was elastic which is a reversible deformation. Figure 3-6 shows the

equivalent plastic strain for each case. The least plastic deformation is for the absorber with foam AF1300 due to its higher strength. Although the difference between the three types were less than 6%. Unlike the conventional rubber systems or coating mechanisms, the suggested sandwich panel design can transform the kinetic energy of projectile to irreversible plastic deformation. This merit will be further explained.



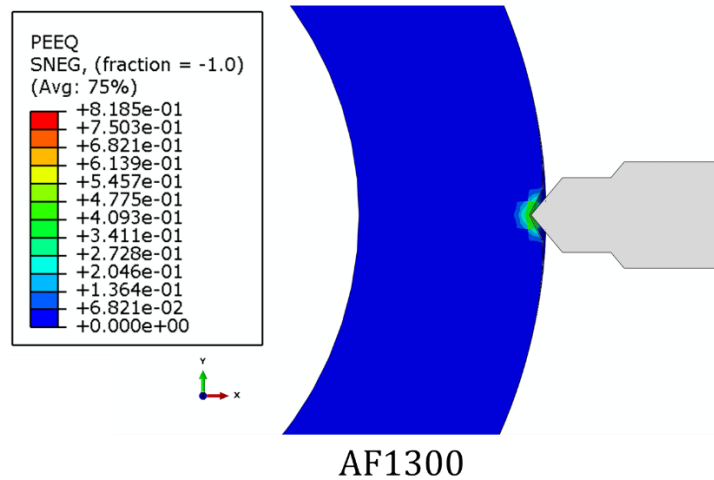


Figure 3-6 Equivalent plastic strain (PEEQ) for each case after the impact

In order to observe the behavior of projectile before, during and after impact the kinetic energy during the impact is plotted versus time, Figure 3-7. It can be seen that the initial impact energy was 35 J and immediately after the initiation of contact with the absorber this value decreases sharply down to zero. At this time majority of kinetic energy has been absorbed by the protective mechanism and the rebounding of the projectile is insignificant. The response of three foams were almost similar with minor differences in rebounding time. The relative difference between final and initial kinetic energy for AF1300 is 82.2%, while this parameter for AF830 and AF630 is approximately equal to 86.2%.

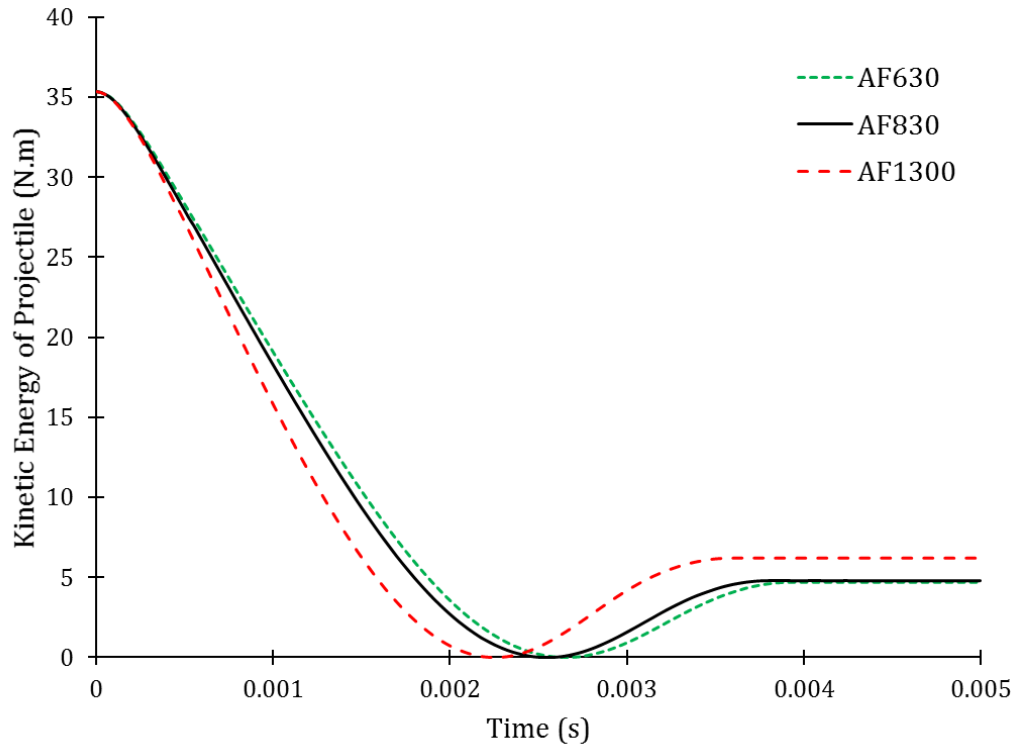


Figure 3-7 Kinetic energy of the projectile during the impact simulation

The plastic dissipated energy of the absorbers is plotted in Figure 3-7 in order to determine the magnitude of energy dissipated by irreversible plastic deformation during the impact. It can be seen that This parameter sharply increases in the response of projectile impact and reaches to its maximum value when the projectile velocity reaches to zero. The final plastic dissipated energy for AF830 and AF630 was higher than that of AF1300 and equal to 25.15 J which is 71.85% of the impact energy. The plastic dissipated energy for AF1300 was 23.20 J which is 8.4% lower than the other absorbers.

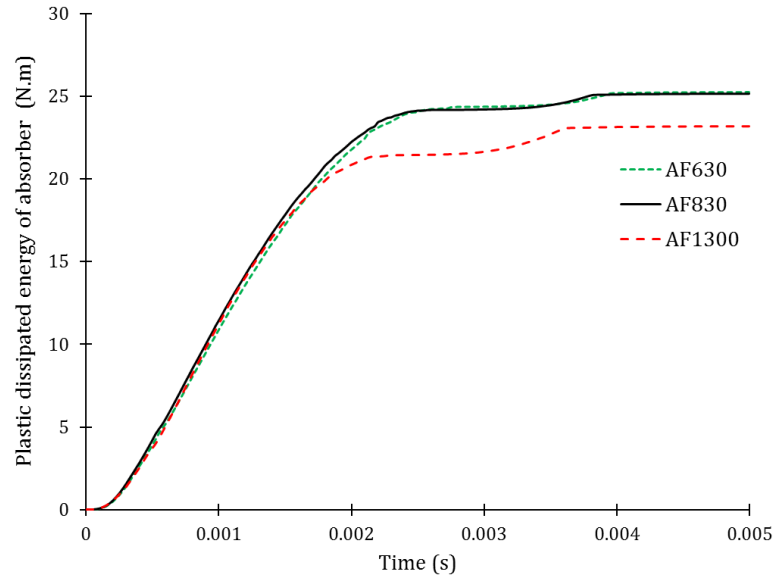


Figure 3-8 Plastic dissipated energy during impact

The variation of projectile velocity during and after the impact can provide useful information about the rebounding and efficiency of absorber to reduce this parameter. The velocity of projectile versus time is plotted in Figure 3-9. It can be seen that the absorbers interestingly reduced the impact velocity and the rebounding velocity by 63 %.

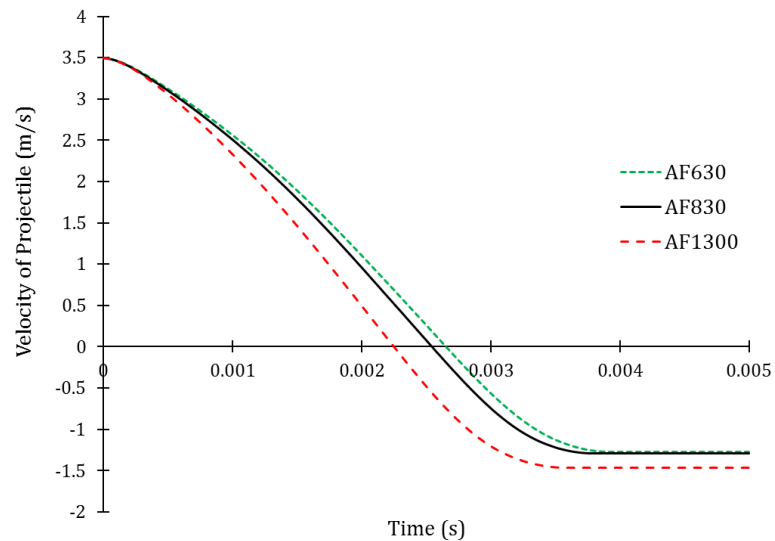


Figure 3-9 Variation of projectile velocity during impact simulation

So far, we observed that the performance of the absorbers with three different cores were almost similar. At the next step of design, we chose the lighter cores by taking out the absorber with core AF1300. Then, we needed to find the optimum thickness for the final design. As it was mentioned before, the allowable thickness of absorber can be up to 50 mm, however, our developed device can be designed slimmer. In order to find the optimum thickness for the absorber we created a path of elements on the absorber on the axis of impact as depicted in Figure 3-10. Afterwards, the final plastic deformation was plotted versus the location on the path. It can be seen that the impact energy is totally dissipated at the depth of 15 mm and there is 35 mm safe zone from which any of the absorbers did not undergo any deformation. Therefore, the final design of absorber can be thinner, and the thickness of minimum 20-35 mm can interestingly absorb the induced impact energy.

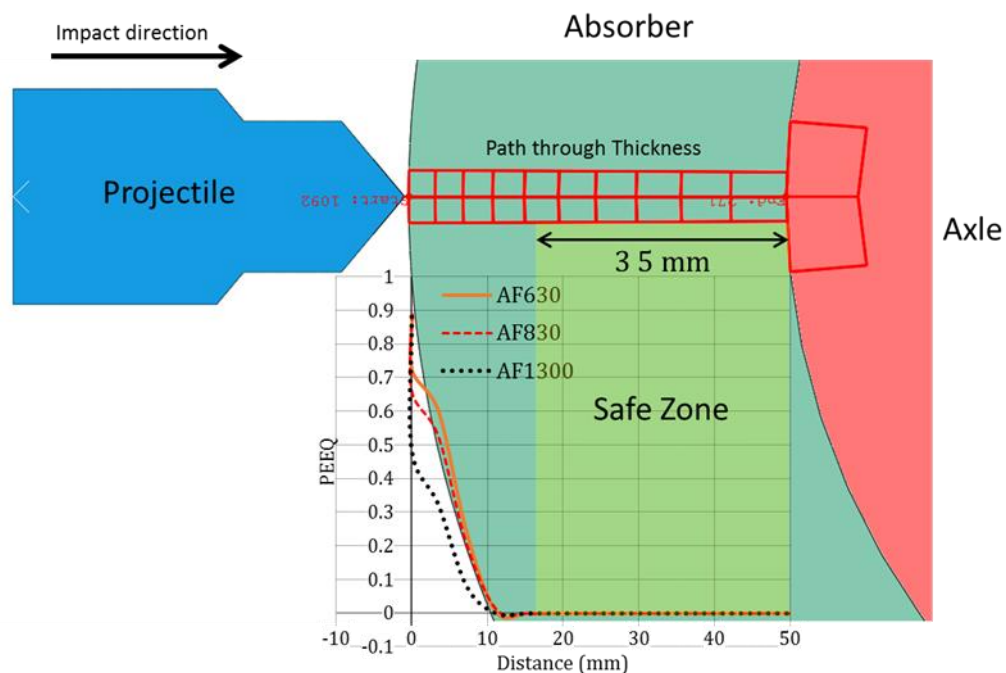
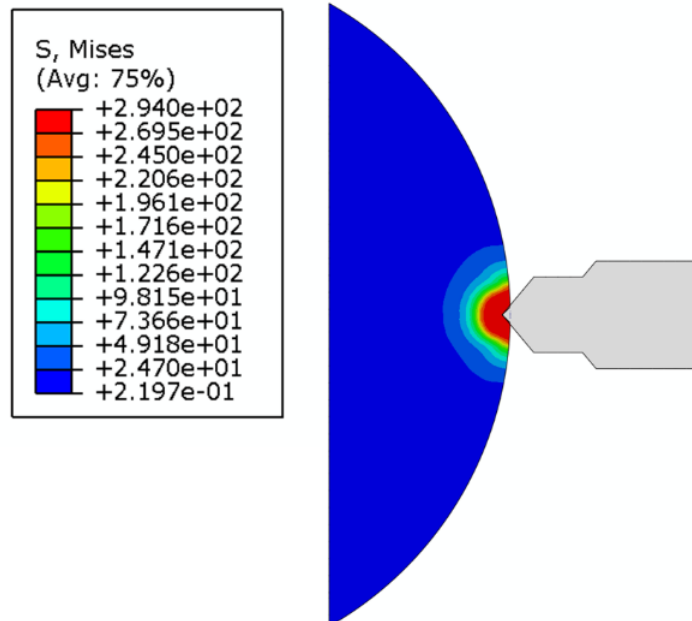


Figure 3-10 PEEQ variation through the thickness of absorber

We also conducted an impact analysis of the bare axle to see the possible damage if there is no absorber attached. Figure 3-11 shows the induced stresses at the impact location which reached to the yield strength of axle. Moreover, the induced plastic strain after the impact illustrates that with the same impact scenario if there is no absorber attached to the axle, there will be perforation, notch and high possibility of crack formation and failure. In our research we considered only radial impact in which the impact direction is perpendicular to the absorber at the location of impact.



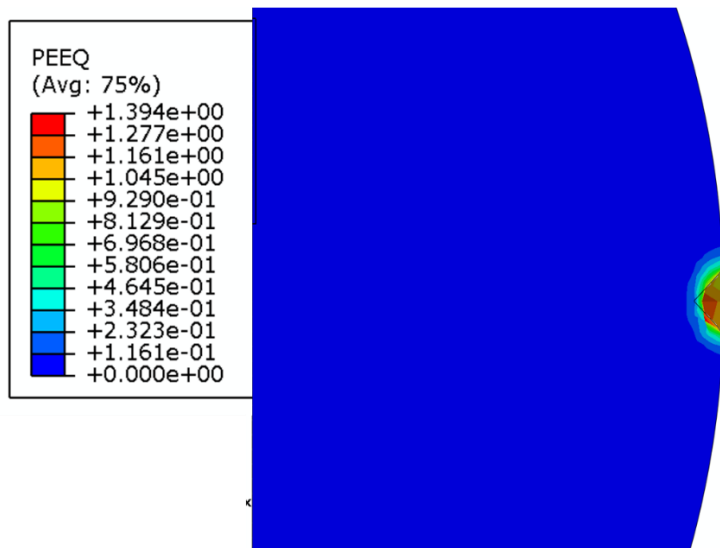


Figure 3-11 The induced stress (top) and PEEQ (bottom) on the axle without absorber

3.4 Experimental tests

We have prepared the sandwich panels to evaluate its performance when exposed to impact. We also made a change and replaced the composite skin with an aluminum skin. The prepared samples are in two groups with different thicknesses and densities. The specifications of samples are listed in Table 3-3 and the test setup is shown in Figure 3-12.

Table 3-3 The sample specifications for experimental tests

| foam thickness [mm] | specimen ID | foam density (kg/m ³) |
|---------------------|-------------|-----------------------------------|
| 20 mm | AF420 | 420 |
| | AF530 | 530 |
| | AF390 | 390 |
| 35 mm | AF640 | 640 |
| | AF560 | 560 |
| | AF520 | 520 |

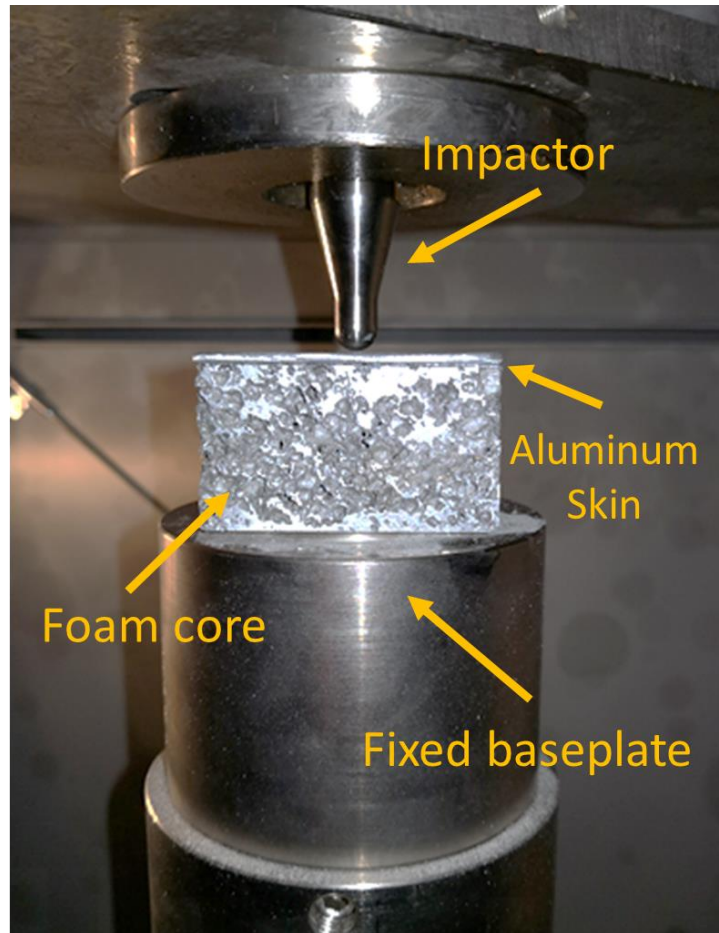


Figure 3-12 The Impact test setup

The critical outputs here were the energy absorption capability, integrity of the structure, and the rebounding of the impactor. The impact energy according to railway standard was set to 35J. Figure 3-13 shows the samples after the impact test. It can be seen that there is not failure of skin or perforation. The skin is locally bended in response of the impact and the sandwich panel absorbed impact energy through irreversible deformation.



Figure 3-13 The cross section of samples with core thickness of 35 mm (top); the samples after impact tests (bottom)

The results of experimental test are plotted in Figure 3-14 and summarized in Table 3-4.

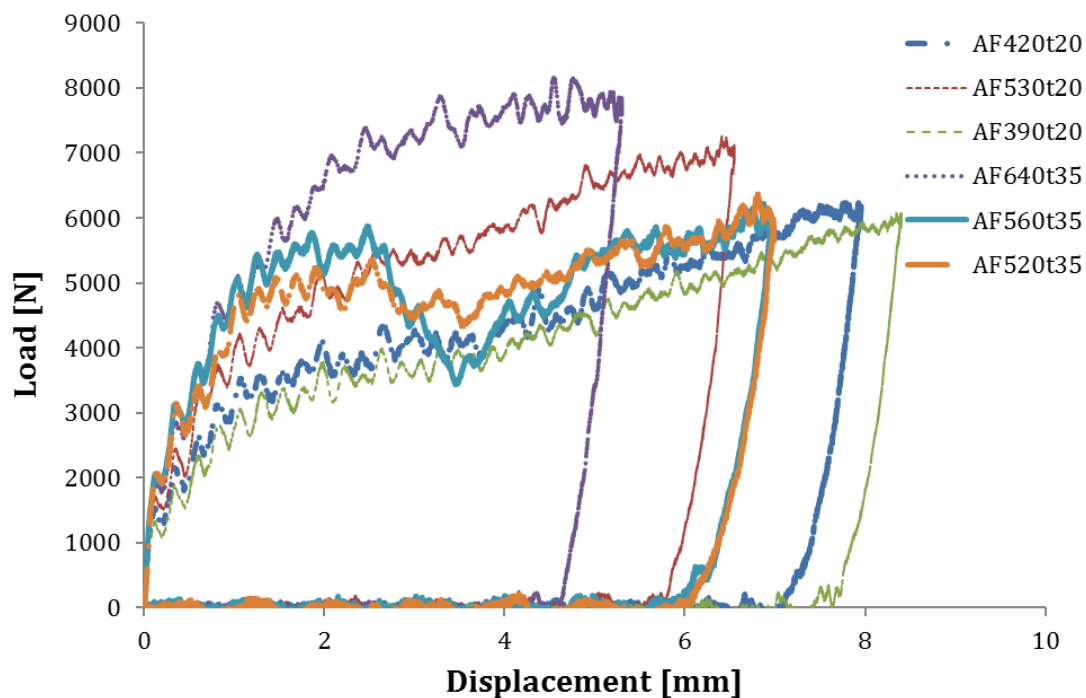


Figure 3-14 Load-displacement curves of the tested sandwich panels

Table 3-4 The results of impact tests

| specimen ID | impact energy [J] | F_{max} [N] |
|-------------|-------------------|---------------|
| AF420t20 | 35 | 6250.4 |
| AF530t20 | 35 | 7257.0 |
| AF390t20 | 35 | 6080.7 |
| AF640t35 | 35 | 8187.6 |
| AF560t35 | 35 | 6221.1 |
| AF520t35 | 35 | 6367.5 |

The velocity of impactor versus impact duration is plotted in Figure 3-15. The velocity of impactor versus impact duration for each case. It can be seen that the initial velocity is 3.5 m/s and sharply decreases when exposed to the protective mechanism and its kinetic energy

after rebounding is decreased by 97 %. Therefore, the mechanism (in all the samples) were able to prevent the projectile from rebounding.

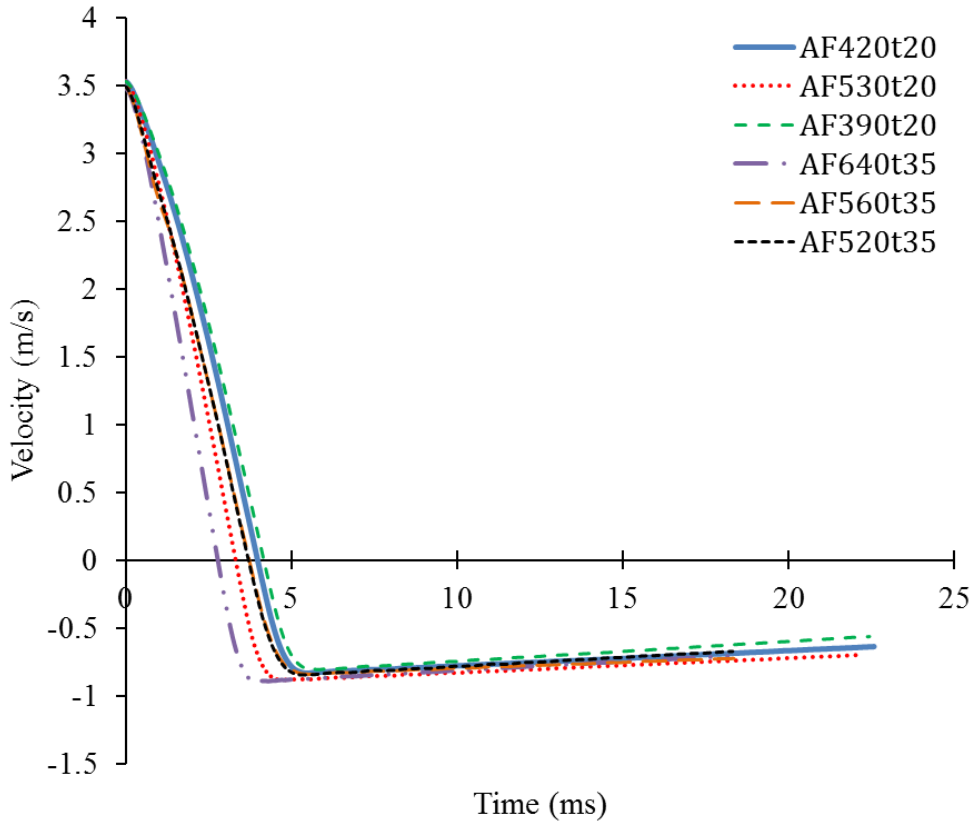


Figure 3-15 The velocity of impactor versus impact duration

Chapter 4: Conclusion and future work

In this research work we have developed two different mechanisms to improve crashworthiness of vehicles and provide protection against ballast impact. We introduced the advantages of double-sided corrugated composite tube over conventional straight metallic tubes. We have demonstrated the performance advantage of the DSC tubes over both SSC and S-tube under axial crushing. Specifically, the absorbed energy of the DSC-14 tube was 330% and 32% higher than that of the SSC tube and S-tube, respectively. However, due to the additional mass in the DSC-14 tube, its specific absorbed energy was 59% lower than that of the S-tube. The change of DSC-14 tube materials from Al 6060-T6 aluminum alloy to CF1263 carbon/epoxy composite laminate could boost its absorbed energy and specific absorbed energy up to 186% and 346% higher than that of the S-tube, respectively. The mechanism of energy absorption for different tube configurations was inspected. The plastic deformation in terms of PPEQ is the key parameter correlating with the energy absorption capacity. Moreover, the influence of number of corrugations on the load-displacement behaviors of the DSC tube was quantified. Results suggested using a thin-walled tube design with minimal straight sections for a controllable smooth crushing behavior, even though minimal straight sections resulted in less SAE. These results could be further verified in crushing experiments of DSC tube, especially composite ones. In addition, the optimization of both geometrical parameters and material properties for the performance of the DSC-tube could be conducted. In summary, the proposed DSC tube might shed light on the design of a thin-walled energy absorber device in transportation industries for mitigation of damages and injuries such as railway industry, Figure 4-1.



Figure 4-1 Application of Double-sided composite corrugated tube in railway application [54]

The next suggested mechanism was ballast impact protection device. We developed finite element models to evaluate the performance of developed sandwich structure in impact energy absorption of projectiles. Our results showed that the initial velocity is 3.5 m/s and sharply decreases when exposed to the protective mechanism and its kinetic energy after rebounding is decreased by 97 %. Therefore, the mechanism (in all the samples) were able to prevent the projectile from rebounding.

Our suggested technology is based on the capabilities of sandwich structure. Here are the benefits of this novel mechanism:

- Less sensitivity to variation of temperature
- Easy installation by using clamping mechanism
- The inner sealing layer protect the axle against corrosion and humidity without any chemical reactions.
- Easy and fast inspection of axle by just unmounting the absorber

- No need to make roughness on the surface of axle
- Absorption of impact energy instead of rebounding the projectile
- Environmentally friendly, as there is no plastic or polymeric component in device. Aluminum is amongst the most environmentally friendly metals on the planet. On a percentage basis, it is the most recycled of any industrial metal.
- The device after its service life can be totally recycled due to the characteristics of its components

We have prepared the sandwich panels to evaluate its performance when exposed to impact. The developed mechanism is able to absorb the impact energy of ballast efficiently. There is an ongoing work about finalizing the design of this device, however our suggestion is to develop to half-tubular shape and attach them by using a clamping system, Figure 4-2.

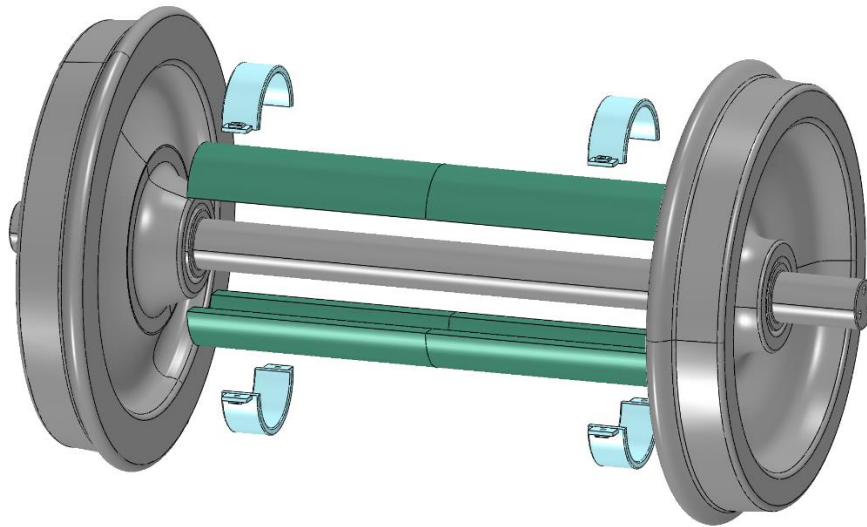


Figure 4-2 The assembly of ballast impact absorber and clamping system

References

1. Jones, N., *Structural impact*. 2011: Cambridge university press.
2. Bambach, M.R., *Fibre composite strengthening of thin-walled steel vehicle crush tubes for frontal collision energy absorption*. *Thin-Walled Structures*, 2013. **66**: p. 15-22.
3. Deb, A., et al., *Design of an aluminium-based vehicle platform for front impact safety*. *International Journal of Impact Engineering*, 2004. **30**(8): p. 1055-1079.
4. Nagel, G., *Impact and energy absorption of straight and tapered rectangular tubes*. 2005, Queensland University of Technology.
5. Ahmad, Z., *Impact and energy absorption of empty and foam-filled conical tubes*. 2009, Queensland University of Technology.
6. Zarei, H. and M. Kröger, *Multiobjective crashworthiness optimization of circular aluminum tubes*. *Thin-walled structures*, 2006. **44**(3): p. 301-308.
7. Boria, S., *13 - Lightweight design and crash analysis of composites*, in *Lightweight Composite Structures in Transport*, J. Njuguna, Editor. 2016, Woodhead Publishing. p. 329-360.
8. Lu, G. and T. Yu, *Energy absorption of structures and materials*. 2003: Elsevier.
9. Zhang, X.W., Q.D. Tian, and T.X. Yu, *Axial crushing of circular tubes with buckling initiators*. *Thin-Walled Structures*, 2009. **47**(6): p. 788-797.
10. Gameiro, C.P. and J. Cirne, *Dynamic axial crushing of short to long circular aluminium tubes with agglomerate cork filler*. *International Journal of Mechanical Sciences*, 2007. **49**(9): p. 1029-1037.
11. Abramowicz, W., *Thin-walled structures as impact energy absorbers*. *Thin-Walled Structures*, 2003. **41**(2): p. 91-107.
12. Abramowicz, W. and N. Jones, *Dynamic axial crushing of circular tubes*. *International Journal of Impact Engineering*, 1984. **2**(3): p. 263-281.
13. Al Galib, D. and A. Limam, *Experimental and numerical investigation of static and dynamic axial crushing of circular aluminum tubes*. *Thin-Walled Structures*, 2004. **42**(8): p. 1103-1137.
14. Guillow, S.R., G. Lu, and R.H. Grzebieta, *Quasi-static axial compression of thin-walled circular aluminium tubes*. *International Journal of Mechanical Sciences*, 2001. **43**(9): p. 2103-2123.
15. Gupta, N.K., *Some aspects of axial collapse of cylindrical thin-walled tubes*. *Thin-Walled Structures*, 1998. **32**(1): p. 111-126.
16. Hanssen, A.G., O.S. Hopperstad, and M. Langseth, *Design of aluminium foam-filled crash boxes of square and circular cross-sections*. *International Journal of Crashworthiness*, 2001. **6**(2): p. 177-188.
17. Hanssen, A.G., M. Langseth, and O.S. Hopperstad, *Static crushing of square aluminium extrusions with aluminium foam filler*. *International Journal of Mechanical Sciences*, 1999. **41**(8): p. 967-993.
18. Meguid, S.A., et al., *Solution stability in the dynamic collapse of square aluminium columns*. *International Journal of Impact Engineering*, 2007. **34**(2): p. 348-359.

19. Jensen, Ø., M. Langseth, and O.S. Hopperstad, *Experimental investigations on the behaviour of short to long square aluminium tubes subjected to axial loading*. International Journal of Impact Engineering, 2004. **30**(8): p. 973-1003.
20. Reid, S.R. and T.Y. Reddy, *Axial crushing of foam-filled tapered sheet metal tubes*. International Journal of Mechanical Sciences, 1986. **28**(10): p. 643-656.
21. El-Hage, H., P.K. Mallick, and N. Zamani, *A numerical study on the quasi-static axial crush characteristics of square aluminum tubes with chamfering and other triggering mechanisms*. International Journal of Crashworthiness, 2005. **10**(2): p. 183-196.
22. Han, D.C. and S.H. Park, *Collapse behavior of square thin-walled columns subjected to oblique loads*. Thin-Walled Structures, 1999. **35**(3): p. 167-184.
23. Mohamed Sheriff, N., et al., *Optimization of thin conical frusta for impact energy absorption*. Thin-Walled Structures, 2008. **46**(6): p. 653-666.
24. Gupta, N.K. and Venkatesh, *Experimental and numerical studies of impact axial compression of thin-walled conical shells*. International Journal of Impact Engineering, 2007. **34**(4): p. 708-720.
25. Hosseini, M., H. Abbas, and N.K. Gupta, *Change in thickness in straight fold models for axial crushing of thin-walled frusta and tubes*. Thin-Walled Structures, 2009. **47**(1): p. 98-108.
26. Gupta, N. and R. Velmurugan, *Axial compression of empty and foam filled composite conical shells*. Journal of composite materials, 1999. **33**(6): p. 567-591.
27. Mamalis, A., et al., *Numerical simulation of thin-walled metallic circular frusta subjected to axial loading*. International Journal of Crashworthiness, 2005. **10**(5): p. 505-513.
28. Singace, A.A., H. El-Sobky, and M. Petsios, *Influence of end constraints on the collapse of axially impacted frusta*. Thin-Walled Structures, 2001. **39**(5): p. 415-428.
29. Mamalis, A.G., et al., *Numerical simulation of thin-walled metallic circular frusta subjected to axial loading*. International Journal of Crashworthiness, 2005. **10**(5): p. 505-513.
30. Gibson, L.J. and M.F. Ashby, *Cellular solids: structure and properties*. 1999: Cambridge university press.
31. De Cooman, B., K. Chin, and J. Kim, *High Mn TWIP steels for automotive applications*. New trends and developments in automotive system engineering, 2011: p. 101-128.
32. Eyvazian, A., et al., *Axial crushing behavior and energy absorption efficiency of corrugated tubes*. Materials & Design (1980-2015), 2014. **54**: p. 1028-1038.
33. Moon, A., et al., *Passivation and corrosion behavior of modified ferritic-pearlitic railway axle steels*. Journal of Materials Engineering and Performance, 2015. **24**(1): p. 85-97.
34. Makino, T., T. Kato, and K. Hirakawa, *Review of the fatigue damage tolerance of high-speed railway axles in Japan*. Engineering Fracture Mechanics, 2011. **78**(5): p. 810-825.
35. Zerbst, U., C. Klinger, and D. Klingbeil, *Structural assessment of railway axles—A critical review*. Engineering Failure Analysis, 2013. **35**: p. 54-65.
36. Beretta, S., A. Ghidini, and F. Lombardo, *Fracture mechanics and scale effects in the fatigue of railway axles*. Engineering fracture mechanics, 2005. **72**(2): p. 195-208.
37. Smith, R. and S. Hillmansen, *A brief historical overview of the fatigue of railway axles*. Proceedings of the Institution of Mechanical Engineers, Part F: Journal of Rail and Rapid Transit, 2004. **218**(4): p. 267-277.
38. Quinn, A., et al., *A full-scale experimental and modelling study of ballast flight under high-speed trains*. Proceedings of the Institution of Mechanical Engineers, Part F: Journal of Rail and Rapid Transit, 2010. **224**(2): p. 61-74.
39. *Protective mechanism for variable*. 1954: USA.

40. Camilla Kontio, H.P., Mats Karlsson *Protection for railway vehicle axle*. 1999, Bombardier Transportation GmbH: USA.
41. Gilles Chretien, E.K., Alain Landrot *Method of protecting a railway vehicle axle, bogie axis and corresponding railway vehicle*. 2003, Alstom Transport SA: Spain.
42. Thierry Guenard, P.T., *Protective film for axles*. 2006, SNCF Mobilites: European Patent Office.
43. Thierry Guenard, P.T., Claude Boccara, Annick Boccara née Houssin *Axle protection membrane*. 2007, Fotia SNCF Mobilites: European Patent Office.
44. José Aitor LANDABEREA RODRÍGUEZ, M.A.I., *Protector for rotary shaft of railway vehicles*. 2016.
45. Шевченко, Г.И.М.М.В.И.Г.А.К.Г., *Protective device for rail vehicle wheel pair axle*. 2014: Russia.
46. Chen, D.-h., *Crush mechanics of thin-walled tubes*. 2015: CRC Press.
47. Mozafari, H., S. Khatami, and H. Molatefi, *Out of plane crushing and local stiffness determination of proposed foam filled sandwich panel for Korean Tilting Train eXpress– Numerical study*. Materials & Design, 2015. **66**: p. 400-411.
48. Obradovic, J., S. Boria, and G. Belingardi, *Lightweight design and crash analysis of composite frontal impact energy absorbing structures*. Composite Structures, 2012. **94**(2): p. 423-430.
49. Hua, Y., P.K. Akula, and L. Gu, *Experimental and numerical investigation of carbon fiber sandwich panels subjected to blast loading*. Composites Part B: Engineering, 2014. **56**: p. 456-463.
50. Gu, L., A.R.M. Kasavajhala, and S. Zhao, *Finite element analysis of cracks in aging aircraft structures with bonded composite-patch repairs*. Composites Part B: Engineering, 2011. **42**(3): p. 505-510.
51. Mondal, D.P., M.D. Goel, and S. Das, *Compressive deformation and energy absorption characteristics of closed cell aluminum-fly ash particle composite foam*. Materials Science and Engineering: A, 2009. **507**(1): p. 102-109.
52. Roven, H.J., et al., *Mechanical properties of aluminium alloys processed by SPD: Comparison of different alloy systems and possible product areas*. Materials Science and Engineering: A, 2005. **410-411**: p. 426-429.
53. Zerbst, U., et al., *The development of a damage tolerance concept for railway components and its demonstration for a railway axle*. Engineering Fracture Mechanics, 2005. **72**(2): p. 209-239.
54. Xie, S., et al., *Crashworthiness optimisation of a composite energy-absorbing structure for railway vehicles*. Structural and Multidisciplinary Optimization, 2018. **57**(4): p. 1793-1807.
55. Bredesen, A.O., *Corrosion and wear protection of wheel axles on trains*. 2016, NTNU.